Distinct Roles of Myosin-II Isoforms in Cytokinesis under Normal and Stressed Conditions

Okada, Hiroki; Wloka, Carsten; Wu, Jian-Qiu; Bi, Erfei

Published in:
iScience

DOI:
10.1016/j.isci.2019.03.014

Publication date:
2019

iScience

CellPress

Article

Distinct Roles of Myosin-II Isoforms in Cytokinesis under Normal and Stressed Conditions

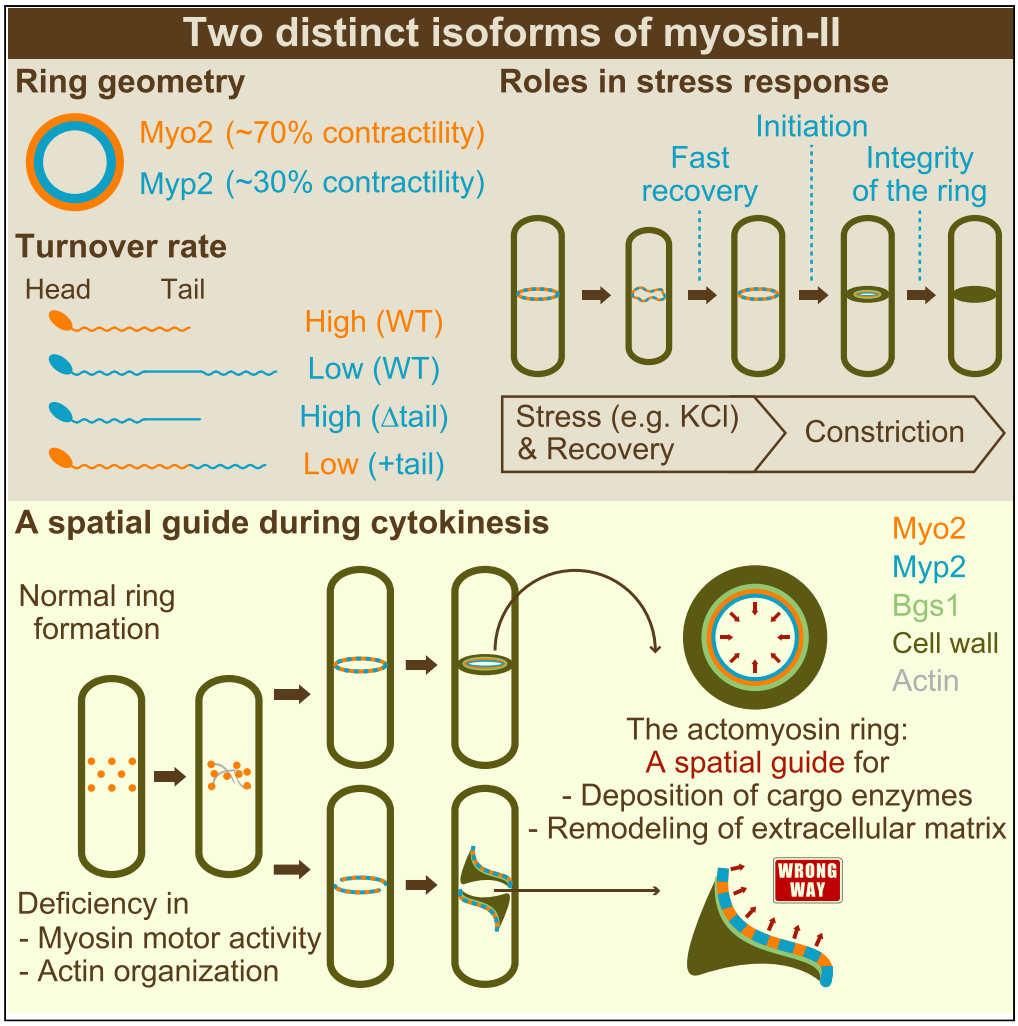

Hiroki Okada, Carsten Wloka, Jian-Qiu Wu, Erfei Bi

ebi@pennmedicine.upenn.edu

HIGHLIGHTS

The myosin-II isoforms Myo2 and Myp2 display distinct responses to cellular stress

Myp2 controls the constriction initiation of Myo2 during stress response

A C-terminal region of Myp2 is required for its immobility during cytokinesis

Myo2 and Myp2 are differentially required for guiding ECM remodeling during cytokinesis

Okada et al., iScience *14*, 69–87
April 26, 2019
https://doi.org/10.1016/j.isci.2019.03.014

iScience

CellPress

Article

Distinct Roles of Myosin-II Isoforms in Cytokinesis under Normal and Stressed Conditions

Hiroki Okada,[1,4] Carsten Wloka,[1,2,4] Jian-Qiu Wu,[3] and Erfei Bi[1,5,*]

SUMMARY

To address the question of why more than one myosin-II isoform is expressed in a single cell to drive cytokinesis, we analyzed the roles of the myosin-II isoforms, Myo2 and Myp2, of the fission yeast *Schizosaccharomyces pombe*, in cytokinesis under normal and stressed conditions. We found that Myp2 controls the disassembly, stability, and constriction initiation of the Myo2 ring in response to high-salt stress. A C-terminal coiled-coil domain of Myp2 is required for its immobility and contractility during cytokinesis, and when fused to the tail of the dynamic Myo2, renders the chimera the low-turnover property. We also found, by following distinct processes in real time at the single-cell level, that Myo2 and Myp2 are differentially required but collectively essential for guiding extracellular matrix remodeling during cytokinesis. These results suggest that the dynamic and immobile myosin-II isoforms are evolved to carry out cytokinesis with robustness under different growth conditions.

INTRODUCTION

The ultimate goal of cytokinesis, the last step of cell division, is to achieve membrane closure between the daughter cells. In animal and fungal systems, cytokinesis involves spatiotemporally coordinated functions of a contractile actomyosin ring (AMR), targeted membrane deposition, and localized extracellular matrix (ECM) remodeling (Balasubramanian et al., 2004; Willet et al., 2015; Bhavsar-Jog and Bi, 2017; Pollard, 2017). The AMR is thought to produce a contractile force that drives furrow ingression, and, in yeast, also to guide membrane position and septum formation, i.e., specialized cell wall synthesis at the division site (equivalent of ECM remodeling in animal cells) (Vallen et al., 2000; Schmidt et al., 2002; Fang et al., 2010; Proctor et al., 2012; Wloka et al., 2013). Targeted membrane deposition increases the surface at the division site and also delivers synthetic and hydrolytic cargo enzymes for septum formation and breakdown, respectively, during cytokinesis (Colman-Lerner et al., 2001; VerPlank and Li, 2005; Zhang et al., 2006). Septum formation in fungi or ECM remodeling in animals is required for stabilizing the AMR during its constriction (Schmidt et al., 2002; VerPlank and Li, 2005; Xu and Vogel, 2011). Septum formation also provides a constrictive force for furrow ingression (Lord et al., 2005; Fang et al., 2010; Proctor et al., 2012). Despite the identification of numerous proteins involved in different aspects of cytokinesis, major questions regarding their assembly, function, and coordination in time and space remain largely unanswered.

For example, it remains unclear why more than one non-muscle myosin-II isoform is expressed in a single cell to drive cytokinesis. Are they required for different steps of cytokinesis? Are they required for fine-tuning force production? Are they required for cells to cope with different cellular stresses? Is the sole function of myosin-II to generate a contractile force that powers the ingression of the cleavage furrow? These fundamental questions regarding the role of myosin-II in cytokinesis can be ideally addressed in the fission yeast *Schizosaccharomyces pombe*. This yeast possesses two non-muscle myosin-II isoforms encoded by the essential and non-essential genes *myo2*$^+$ and *myp2*$^+$/*myo3*$^+$ (hereafter *myp2*$^+$), respectively (Kitayama et al., 1997; Motegi et al., 1997; Bezanilla et al., 1997); displays stereotyped behaviors in cytokinesis, including the behaviors of the AMR and primary septum (PS) formation (Balasubramanian et al., 2004; Pollard and Wu, 2010; Willet et al., 2015); and is amenable to genetic analysis and live-cell imaging. Although the basic properties and mutant phenotypes of Myo2 and Myp2 have been characterized (Bezanilla et al., 2000; Motegi et al., 2000; Takaine et al., 2015; Laplante et al., 2015; Palani et al., 2017), the underlying mechanisms remain elusive. For example, it is known that Myo2 is highly dynamic, whereas Myp2 is immobile during cytokinesis (Pelham and Chang, 2002; Wloka et al., 2013; Takaine et al., 2015), but what

[1]Department of Cell and Developmental Biology, Perelman School of Medicine, University of Pennsylvania, Philadelphia, PA 19104-6058, USA

[2]Groningen Biomolecular Sciences and Biotechnology Institute, University of Groningen, 9747 AE Groningen, The Netherlands

[3]Department of Molecular Genetics, The Ohio State University, Columbus, OH 43210, USA

[4]These authors contributed equally

[5]Lead Contact

*Correspondence: ebi@pennmedicine.upenn.edu

https://doi.org/10.1016/j.isci.2019.03.014

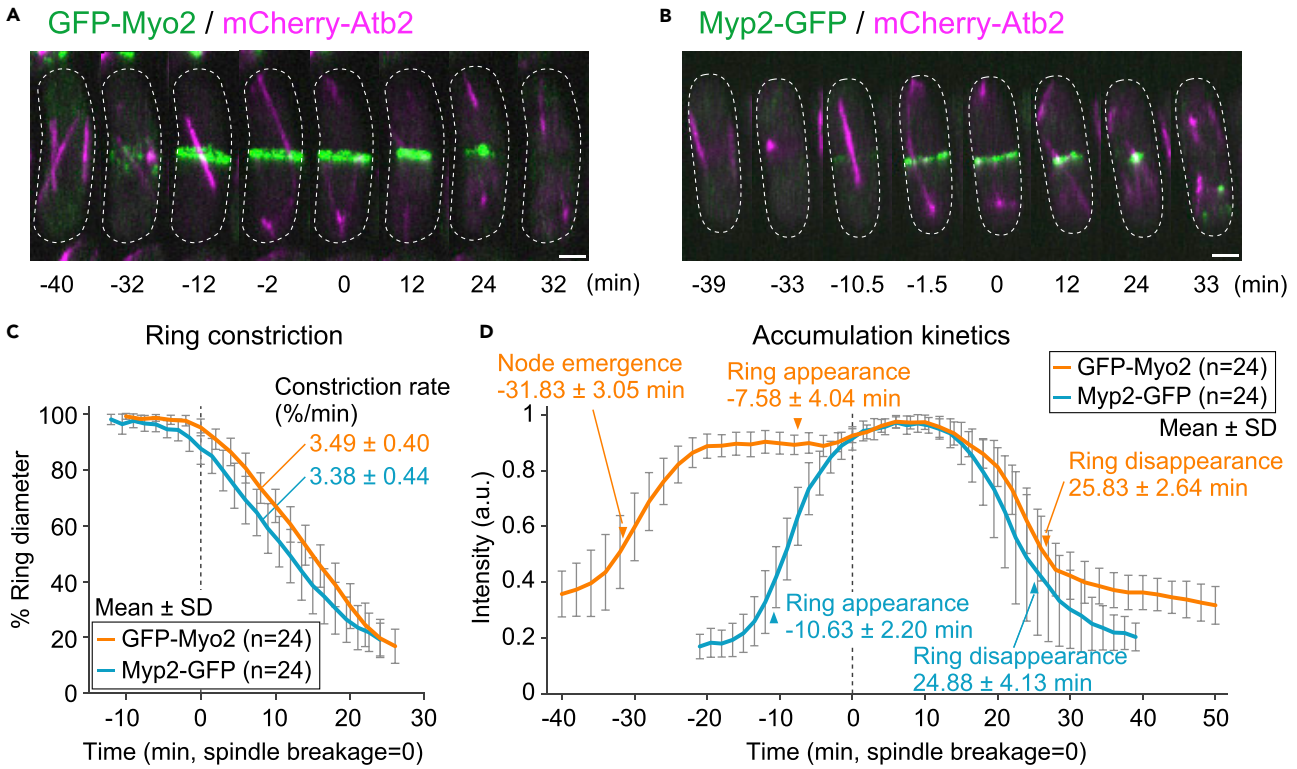

Figure 1. Myo2 and Myp2 Display Distinct Localization Patterns during Cytokinesis

(A and B) Localizations of Myo2 and Myp2. Time-lapse analysis of myosin-II isoforms Myo2 (A) and Myp2 (B) in *S. pombe* was performed on cells of WT strains (YCW0130: *GFP-myo2 mCherry-atb2*) and (YCW0018: *myp2-GFP mCherry-atb2*). Imaging data on individual cells were aligned according to the spindle-breakage point (the spindle was labeled by mCherry-Atb2, a tubulin subunit). See also Video S1. Scale bar, 2 μm.

(C and D) Constriction (C) and accumulation (D) kinetics of Myo2 and Myp2. Imaging data from (A and B) were analyzed. See also Figure S1, and Video S2.

accounts for the difference remains unknown. It is known that *myp2Δ*, but not *myo2-E1*, cells are hypersensitive to high salt at low temperatures (Bezanilla et al., 2000), but how Myo2 and Myp2 behave under such a stress has not been examined. Although significant progress has been made in the study of the AMR and PS formation, their functional relationship has remained unclear.

In this study, we have identified a molecular determinant for the turnover difference between Myo2 and Myp2 during cytokinesis, discovered that Myp2 is required for the timely disassembly and constriction of the Myo2 ring in response to high-salt stress, and found that Myo2 and Myp2 are differentially required and collectively essential for guiding PS formation during cytokinesis, and this guiding role can occur independently of myosin-II motor activity.

RESULTS

Myo2 and Myp2 Display Distinct Localization Patterns and Accumulation Kinetics during Cytokinesis

To address the question of why more than one myosin-II isoform is expressed in a single cell to drive cytokinesis, we first compared the localization patterns and accumulation kinetics of GFP-Myo2 and Myp2-GFP in fission yeast during the cell cycle using mitotic spindle length (mCherry-Atb2) as the cell-cycle marker (Ding et al., 1998; Nabeshima et al., 1998; Bezanilla et al., 2000). In all experiments except where noted, the timing of spindle breakage was taken as the reference point for the description and quantification of cellular events involved in cytokinesis. Dual-color time-lapse analysis indicated that Myo2 localized to the cell equator as a cloud of nodes associated with the plasma membrane at the onset of mitosis when all the interphase microtubules were disassembled and a "spot-like" mitotic spindle was formed within the nucleus (Figure 1A, and Video S1), as *S. pombe* undergoes closed mitosis. Myo2 nodes then coalesced

into a ring-like structure during metaphase and anaphase A when the spindle elongated from 0 to ~2.7 μm. The Myo2 ring retained and "matured" at the division site during anaphase B when the spindle elongated from ~2.7 to ~13 μm. The Myo2 ring started to constrict slowly shortly before the spindle breakage and then constricted rapidly with a nearly constant rate immediately after the spindle breakage (Figures 1A and 1C, and Video S1). In contrast, Myp2 did not form nodes and began to accumulate at the cell equator during anaphase B when the spindle was ~6.5 μm long (Figure 1B and Video S1). The Myp2 ring started a slow phase of constriction slightly earlier than the Myo2 ring did (Figure 1C), which was followed by a fast phase of constriction (Figures 1B and 1C). The offset in the initiation of the ring constriction for Myp2 and Myo2 presumably explains the spatial segregation of the myosin-II isoforms during cytokinesis, as observed by time-lapse analysis of cells carrying Myp2-mCherry and GFP-Myo2 (Figure S1, and Video S2), which confirms previous reports (Laplante et al., 2015; McDonald et al., 2017).

Strikingly, Myo2 and Myp2 at the division site were still at their peak levels (Figure 1D, 6-8 min) even after the initiation of their fast-phase constriction (Figures 1C and 1D, 0 min). This is similar to the behavior of Mlc1, the essential light chain in the budding yeast *Saccharomyces cerevisiae*, during cytokinesis (Feng et al., 2015). This continuous increase during ring constriction may endow cytokinesis with robustness against stresses or perturbations, a point that will be discussed in a later section. The overall timing of Myo2 and Myp2 localization with respect to the spindle behavior during the cell cycle, as revealed in this study, was consistent with a previous report (Bezanilla et al., 2000). Our data, together with previous studies (Bezanilla et al., 2000; Motegi et al., 2000; Wu et al., 2003; Laplante et al., 2015), indicate that Myo2 and Myp2 display distinct localization patterns and accumulation kinetics at the division site during the cell cycle.

Myp2 Is Required for the Disassembly, Stability, and Constriction Initiation of the Myo2 Ring during Stress Response

The distinct localization patterns of Myo2 and Myp2 suggest that the myosin-II isoforms may play distinct roles in cytokinesis. To test this possibility, we first examined the molecular behavior of Myo2 and Myp2 during stress response, as a previous report indicates that cells carrying a deletion of *myp2* (*myp2*Δ), but not a temperature-sensitive mutation of *myo2* (*myo2-E1*), are inviable and display defects in cytokinesis in the presence of high salt (1 M KCl) (Bezanilla and Pollard, 2000). Upon the addition of 1 M KCl, a pre-formed Myo2 ring in wild-type (WT) cells shrunk quickly, presumably due to high osmotic pressure (Figure 2A and Video S3). The ring disassembled without constriction (~37.5 min after KCl addition; designated here the "initial osmotic response"), then reassembled into an intact ring (~52.5 min; designated the "recovery" phase) that subsequently underwent constriction (designated the "adaptive" phase) (Figures 2A and 2D). For interphase cells, the addition of KCl triggered cytoplasmic shrinkage that was accompanied by the formation of Myo2 "puncta" (Figure 2A and Video S3). This stress response lasted ~37.5 min, and then cells recovered, as manifested by the return of cytoplasmic volume to normal and the disappearance of the Myo2 puncta. Similar to Myo2, a pre-formed Myp2 ring shrunk right after the addition of KCl, but, in contrast, the ring started to disassemble and move away from the division site as puncta or "cable-like" structures (Figure 2B and Video S3). The disassembly process lasted ~30–37.5 min, which was not followed by recovery and constriction (Figure 2B and Video S3). For the interphase cells, the cytoplasmic shrinkage was not accompanied by the formation of Myp2 puncta (Figure 2B and Video S3). Thus, Myo2 and Myp2 clearly display distinct behaviors in response to high-salt stress.

To determine whether the response was caused by osmolarity, charge, or both of the high salt concentration, we performed the same experiments using 2 M sorbitol instead of 1 M KCl (both solutions have the same osmolarity). Similar to the high-salt treatment, the pre-formed Myo2 ring went through the process of disassembly, reassembly, and constriction upon sorbitol addition (Figures S2A and S2D, and Video S3). Interphase cells went through a similar process of cytoplasmic shrinkage-recovery that was accompanied by the formation-disappearance of Myo2 puncta. The pre-formed Myp2 ring also went through a similar process of quick shrinkage and disassembly, but, in contrast, this was followed by recovery and constriction (Figures S2B and S2D, 75min; and Video S3). Myp2 in interphase cells behaved similarly under both stressed conditions. In addition, it is noteworthy that during the disassembly and reassembly process, Myp2, but not Myo2, was associated with the post-anaphase array (PAA) of microtubules under both stressed conditions (Figures 2B and S2B). This is consistent with the demonstrated interaction between Myp2 and the PAA-associated protein Mto1 and also with the requirement of Myp2 for PAA formation (Samejima et al., 2010). Together, these data suggest that the disassembly of

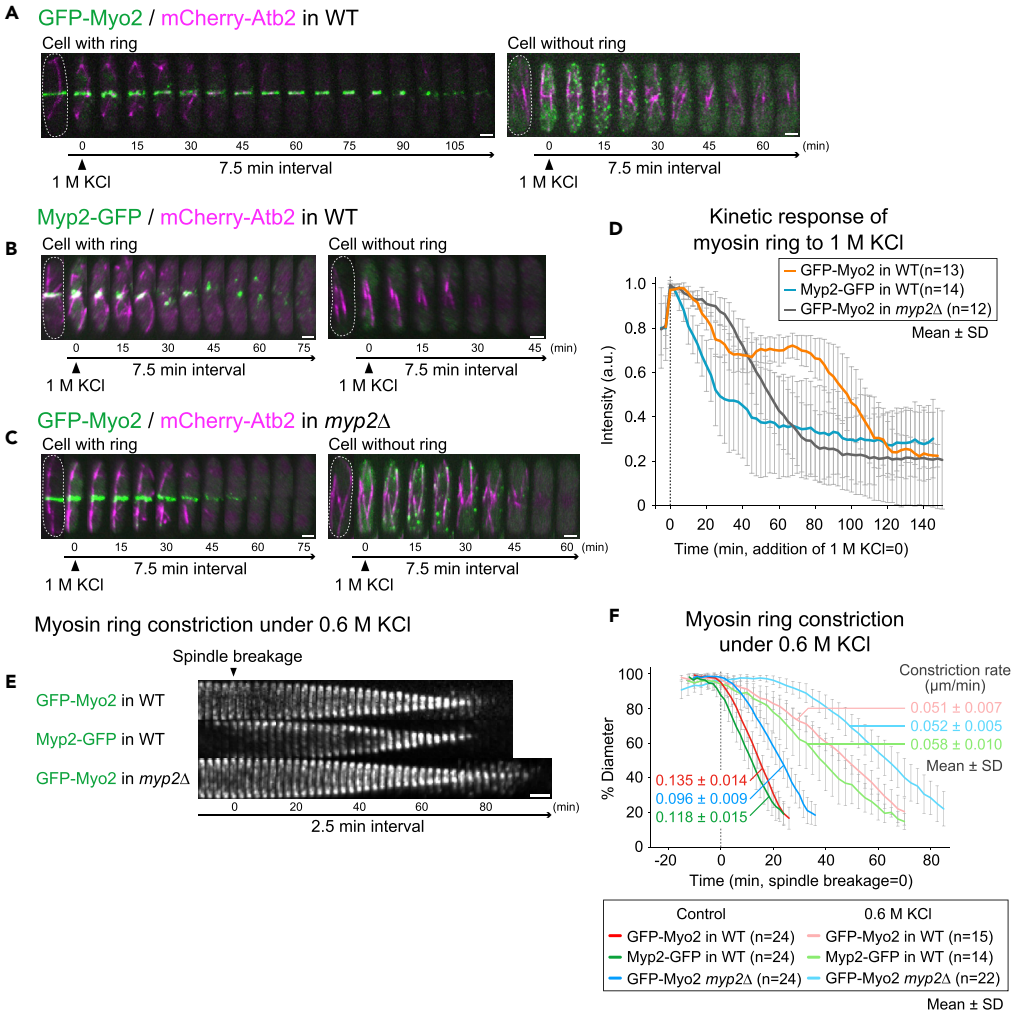

Figure 2. Myp2 Is Required for the Timely Disassembly, Stability, and Constriction Initiation of the Myo2 Ring during Stress Response to High Salt

(A–D) The behaviors of pre-formed Myo2 and Myp2 rings in dividing cells as well as of Myo2 and Myp2 in interphase cells in response to 1 M KCl treatment. Time-lapse analysis Myo2 (A), Myp2 (B), and Myo2 in *myp2*Δ (C) was performed on cells of WT strains (YCW0130 and YCW0018) and *myp2*Δ strain (YCW0073: *myp2*Δ *GFP-myo2 mCherry-atb2*). During live imaging, culture medium was changed from YE5S to YE5S containing 1 M KCl to induce the high-salt stress response. The intensities of Myo2 and Myp2 at the division site from the imaging data as described in Panels A–C are quantified and presented here (D).

(E) The behaviors of *de novo*-formed Myo2 and Myp2 rings in dividing cells in response to 0.6 M KCl treatment. The same strains and live-cell imaging were performed except that the salt concentration was 0.6 M instead of 1 M KCl to maintain the viability of *myp2*Δ cells.

(F) The kinetics of constriction for the *de novo*-formed Myo2 rings in different strains in the presence of 0.6 M KCl were determined and presented here (F).

Scale bar, 2 μm. See also Figures S2 and S3, Videos S3 and S4, and Table S1.

both Myo2 and Myp2 is caused by high osmolarity, but Myp2, not Myo2, reassembly is inhibited specifically by high salt.

Because the growth and division of *myp2*Δ cells are hypersensitive to high salt (Bezanilla and Pollard, 2000), we reasoned that the Myo2 behavior might be affected under this condition. To test this possibility, we performed time-lapse microscopy of GFP-Myo2 in *myp2*Δ cells in the presence of 1 M KCl. Strikingly, the pre-formed Myo2 ring failed to disassemble during the first 37.5 min after the addition of KCl, which was followed by gradual disassembly without constriction (Figures 2C and 2D; and Video S3, 75 min).

Upon the addition of 2M sorbitol, the pre-formed Myo2 ring also showed delayed disassembly; however, in this case, it was followed by reassembly into a ring structure that displayed a highly aberrant constriction (Figure S2C). The ring was slanted (14 of 36 rings), zigzag in shape (31 of 36 rings), and/or constricted asymmetrically (11 of 36 rings). Cable-like structures protruded from the constricting ring, suggesting that the integrity of the Myo2 ring is compromised under this condition (Figure S2C, and Video S3). Together, these data indicate that Myp2 is required for the timely disassembly of the Myo2 ring during the initial osmotic response as well as for the integrity of the Myo2 ring during the adaptive phase.

To gain further insight into the regulation of Myo2 by Myp2 under stress condition, we analyzed Myo2 and Myp2 behaviors in the presence of 0.6 M KCl to avoid the lethality caused by 1 M KCl to *myp2*Δ cells, as shown previously by plate assay (Bezanilla and Pollard, 2000). Under this condition, Myo2 and Myp2 in WT cells as well as Myo2 in *myp2*Δ cells harboring a pre-formed ring or in interphase displayed stereotypical behaviors as seen in the presence of 2 M sorbitol (Figure S3). The presence of 0.6 M KCl did not prevent the de novo formation of Myo2 or Myp2 ring (Figure 2E and Video S4) but decreased the rate of constriction for the newly formed Myo2 rings in WT and *myp2*Δ cells to 37.8% and 54.2% of the rates of the same strains in the absence of 0.6 M KCl, respectively (Figure 2F and Table S1). Strikingly, the onset of constriction was significantly delayed in *myp2*Δ cells in the presence of the salt (~20 min after spindle breakage) to that in the absence of the salt (~0 min). In contrast, the WT cells did not show any obvious difference in the onset of constriction (~2.5 min) regardless of the presence of the salt. These data indicate that Myp2 is required for the timely initiation of the Myo2 ring constriction under high-salt stress.

Collectively, these data indicate that Myo2 and Myp2 display distinct responses to high-osmolarity or high-salt stress and that Myp2 is required for the dynamic disassembly, stability, and constriction initiation of the Myo2 ring during stress response.

A C-Terminal Region of Myp2 Is Essential for Its Immobility and Contractility during Cytokinesis

Certain myosin-II isoforms such as Myo2 in fission yeast (Pelham and Chang, 2002) and the non-muscle myosin-IIA in mammalian cells (Kondo et al., 2011) display high turnover rates during cytokinesis. In contrast, Myo1, the sole myosin-II heavy chain in *S. cerevisiae* (Dobbelaere and Barral, 2004; Wloka et al., 2013) and myosin-II in *Drosophila* S2 cells (Uehara et al., 2010) are immobile during cytokinesis. To explore this apparent paradox, we directly compared the dynamics of Myo2 and Myp2 in fission yeast using the fluorescence recovery after photo bleaching (FRAP) approach. As expected, Myo2 was highly dynamic (maximal recovery: 34.5 ± 1.9%; $T_{1/2}$: 31.2 ± 4.9 s; n = 20) (Pelham and Chang, 2002), whereas Myp2 was largely immobile during cytokinesis (max: 59.3 ± 14.3%; $T_{1/2}$: 256.2 ± 56.9 s; n = 18) (Figures 3A–3C, S4A, and S4D, and Video S5) (Wloka et al., 2013; Takaine et al., 2015). Collectively, our data indicate that different myosin-II isoforms in fission yeast display distinct turnover during cytokinesis.

To determine the mechanism and function underlying Myp2 immobility, we made two C-terminally truncated, GFP-tagged alleles of *myp2*$^+$, *myp2-(1–1,621)* and *myp2-(1–1922)* (Figure 3A). The truncated products are predicted to lack nearly the entire second CC region in Myp2 tail or a small C-terminal portion of this region (Figure 3A) (Bezanilla and Pollard, 2000). This experiment was designed based on our previous observation in budding yeast that deletion of a C-terminal region of Myo1 abolishes its immobility and the truncation allele displays synthetic lethality with the deletion of *HOF1* that encodes an F-BAR protein involved in cytokinesis (Wloka et al., 2013). The boundaries of the Myp2 truncations were determined by an educated guess based on poorly but detectable sequence conservation between Myp2 and other non-muscle myosin-IIs from different organisms (*S. cerevisiae*, other fungi, human, and mouse). Remarkably, both truncations, Myp2-(1-1,621) (max: 51.3 ± 3.1%; $T_{1/2}$: 62.0 ± 10.8 s; n = 27) and Myp2-(1-1922) (max: 47.6 ± 3.9%; $T_{1/2}$: 104.2 ± 7.9 s; n = 28), converted Myp2 from an immobile to a mobile state, as the $T_{1/2}$ of each truncation was shorter than that of Myp2, and clear molecular exchange was observed between the bleached and unbleached halves for either truncation but not for the WT Myp2 (Figures 3C–3E, and S4A-4C, and Video S5). Importantly, Myp2-(1-1,621) recovered more quickly than Myp2-(1-1922), as indicated by their $T_{1/2}$ values (Figure S4), suggesting that the former resembles Myo2 more than the latter does. Together, these data suggest that the second CC region is required for maintaining Myp2 immobility during cytokinesis.

To determine the function of the second CC region of Myp2 in cytokinesis, we spotted 10-fold serial dilutions of the strains carrying the *myp2*$^+$, *myp2-(1–1,621)*, *myp2-(1–1922)*, and *myp2Δ*, on plates with or

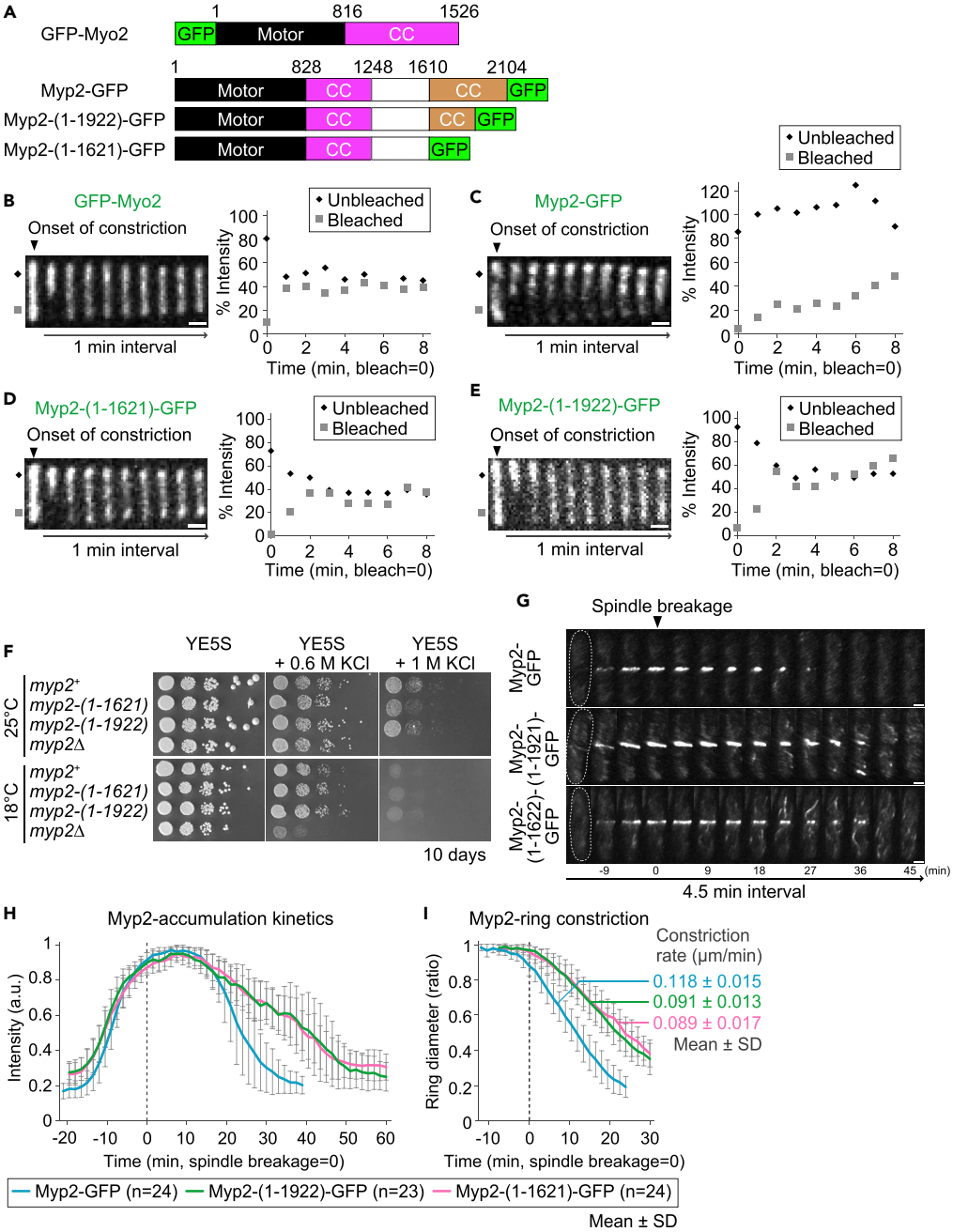

Figure 3. A C-Terminal Coiled-Coil Region of Myp2 Is Required for Its Immobility and Function but Dispensable for Localization

(A) Schematic of Myo2 and Myp2 domains and Myp2 C-terminal truncations. "Motor," "CC" in magenta box, and "CC" in brown box indicate the motor domain, first coiled-coil domain, and second coiled-coil domain of the indicated myosin-II isoform, respectively.

(B–E) Fluorescence recovery after photobleaching (FRAP) analysis of Myo2 and Myp2 as well as C-terminally truncated Myp2. FRAP analysis was performed on cells of WT strains (YCW0130) (B) and (YCW0017: *myp2-GFP mCherry-atb2*) (C) and *myp2* truncation strains [YCW0031: *myp2-(1–1,621)-GFP mCherry-atb2* (D) and YCW0032: *myp2-(1–1922)-GFP mCherry-atb2* (E)] to determine the relative turnover rates of myosin-II during cytokinesis. A half of the ring from cells was photo-bleached, and fluorescence recovery in the bleached and unbleached regions was followed over time. See also Figure S4 and Video S5. Scale bar, 1 μm.

Figure 3. *Continued*

(F) Growth of strains of WT (YCW0015: *myp2-GFP*), *myp2-(1–1,621)* [YCW0029: *myp2-(1–1,621)-GFP*], *myp2-(1–1922)* [YCW0030: *myp2-(1–1922)-GFP*], and *myp2Δ* (YCW0054: *myp2Δ*) was examined on YE5S plate with or without potassium chloride.

(G) Localizations of truncated Myp2 proteins. See also Video S1. Scale bar, 2 μm.

(H and I) Accumulation (H) and constriction (I) kinetics of WT and truncated Myp2 proteins. Imaging data from (G) were analyzed and plotted.

See also Figure S5.

without high salt. As expected, *myp2Δ* cells failed to grow on plates containing 1 M KCl at 25°C (Figure 3F) (Bezanilla and Pollard, 2000). We also found that *myp2Δ* cells failed to grow on plates containing 0.6 M KCl at 18°C (Figure 3F). In contrast, cells carrying either of the *myp2* truncation alleles grew like the WT cells on plates containing either 0.6 or 1 M KCl at 25 or18°C (Figure 3F). Thus, the second CC region or the immobility of Myp2 is dispensable for its essential role in cell survival under high salt at low temperatures.

To explore the function of the second CC region further, we tested whether the truncation alleles of *myp2* displayed genetic interactions with other mutations affecting cytokinesis at different temperatures (23°C, 25°C, 30°C, 32°C, and 36°C). Like the WT strain, cells carrying either of the truncation alleles were able to grow well at all temperatures examined (Table S2). However, both truncation alleles were synthetically lethal or sick with a number of mutations affecting cytokinesis, including *cdc4-s16* (Wu et al., 2010), *myo2-E1* (Balasubramanian et al., 1998; Bezanilla and Pollard, 2000), *cdc11-123* (Bezanilla et al., 1997), and *myo51Δ* (Laplante et al., 2015) (Table S2). This result suggests that the second CC region of Myp2 is important for its function.

To determine the molecular defects of the truncation alleles, we imaged both mutants throughout the cell cycle, and found that both Myp2-(1-1,621) and Myp2-(1-1922) accumulated at the division site with the same kinetics as the WT Myp2 did (Figures 3G and 3H, and Video S1). This is consistent with the previous observation that localization of Myp2 to the division site is largely determined by its motor domain (Takaine et al., 2015). However, both truncations caused a similar delay in their removal from the division site (Figures 3G and 3H) and also a similar decrease in ring constriction (Figure 3I). Strikingly, both truncated proteins formed "cable-like" structures that flew away from the division site during the latter half of the Myp2 ring constriction, with the Myp2-(1-1,621) displaying a more severe phenotype (Figure 3G). Because the overall behaviors of the two truncation alleles were similar, for some analyses hereafter, only the *myp2-(1–1,621)* truncation allele was chosen. As the regulatory light chain Rlc1 is shared by both Myo2 and Myp2 (Naqvi et al., 2000; D'Souza et al., 2001), we monitored the contractile ring in different *myp2* mutants by imaging cells carrying Rlc1-tdTomato (Figure S5). In WT cells, Rlc1 displayed two distinct peaks of accumulation. The second peak was nearly abolished in *myp2Δ* cells (Figure S5A). Thus, the binding of Rlc1 to Myo2 and Myp2 accounts for its first and second peak, respectively. The rate of Rlc1 constriction was reduced by 33.1% in *myp2Δ* cells (Figure S5B and Table S1). This decrease in the rate of Rlc1-tdTomato constriction was comparable with the 29.4% drop in the rate of GFP-Myo2 constriction in *myp2Δ* versus WT cells (Figure 2F and Table S1). Thus, by two independent measures, Myp2 accounts for approximately one-third of the rate for AMR constriction. In *myp2-(1–1,621)* cells, the second peak of Rlc1 accumulation was dampened. Given the normal accumulation kinetics of Myp2-(1–1,621) (Figure S5A), this result suggests that deletion of the second CC region of Myp2 could interfere with Rlc1 binding to its neck region. Surprisingly, the rate of Rlc1 constriction in *myp2-(1–1,621)* cells was reduced to a similar degree (34.5%, Table S1) as in *myp2Δ* cells. These data suggest that the second CC region is essential for the contribution of Myp2 to the overall rate of ring constriction.

In summary, our data, together with previous work (Takaine et al., 2015), indicate that the localization and immobility of Myp2 are mediated by distinct domains, namely, its N-terminal motor domain and its C-terminal second CC region. These domains are responsible for the distinct roles of Myp2 in cell survival under high-salt stress and its immobility during cytokinesis, respectively.

Addition of a C-Terminal Region of Myp2 to the End of Myo2 Confers Myp2-like Features

To further determine the function of the second CC region of Myp2, we made two GFP-tagged *myo2* chimeras, *GFP-myo2-ST* and *GFP-myo2-LT*. These chimeras contained the entire *myo2*$^{+}$ sequence that was fused in-frame with the coding sequence for either the Short Tail (a.a. 1,923–2,104) or the Long Tail (a.a. 1,622–2,104) from the second CC region of Myp2 (Figure 4A). FRAP analysis indicated that

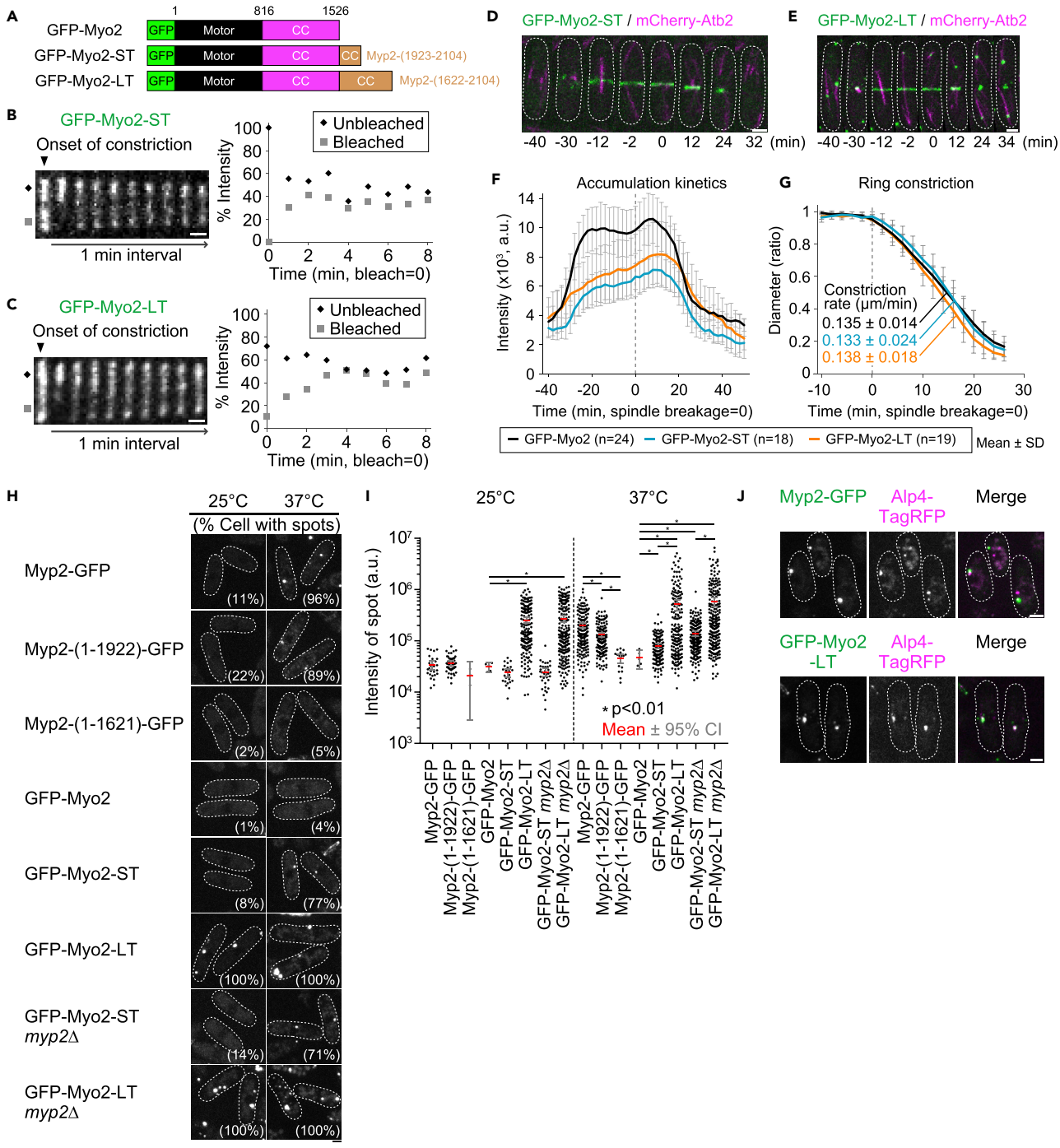

Figure 4. A C-Terminal Fragment of Myp2 Renders Myo2 with Myp2-like Features

(A) Schematic of Myo2 and Myo2-ST (Short Tail from Myp2) and Myo2-LT (Long Tail from Myp2) chimeras.

(B and C) FRAP analysis of Myo2-ST and Myp2-LT. FRAP analysis was performed on cells expressing Myo2-ST [YCW0166: *GFP-myo2-myp2-(1923–2104) mCherry-atb2*] (B) or Myo2-LT [YCW0175: *GFP-myo2-myp2-(1,622–2104) mCherry-atb2*] (C). See also Figure S6 and Video S5. Scale bar, 1 μm.

(D and E) Localization patterns of Myo2-ST and Myo2-LT during the cell cycle. Time-lapse analysis was performed on cells of the *myo2-ST* strain (YCW0166) (D) and *myo2-LT* strain (YCW0175) (E). Scale bar, 2 μm.

(F and G) Accumulation (F) and constriction (G) kinetics of Myo2-ST and Myo2-LT proteins. Imaging data from (D and E) were analyzed and plotted. See also Table S1.

(H) Spot formation by different *myo2* and *myp2* alleles. Cells were grown to early exponential phase in YE5S medium at 25°C and then split into two parts that were grown for additional 6 h at 25°C and 37°C, respectively, before documentation by microscopy. The strains used in this analysis were WT *myp2*$^{+}$

Figure 4. *Continued*

(YCW0125: *myp2-GFP mCherry-atb2*), *myp2-(1–1922)* (YCW0032), *myp2-(1–1,621)* (YCW0031), WT *myo2*$^{+}$ (YCW0130), *myo2-ST* (YCW0166), *myo2-LT* (YCW0175), *myo2-ST myp2*Δ [YCW0190: *myp2Δ GFP-myo2-myp2-(1923–2104) mCherry-atb2*], and *myo2-LT myp2*Δ [YCW0194: *myp2Δ GFP-myo2-myp2-(1,622–2104) mCherry-atb2*]. The percentage of cells containing myosin-II spots was indicated at the bottom-right corner of individual images. For each condition, >90 cells were used for quantification. Scale bar, 2 μm.

(I) Intensities of myosin-II spots. Imaging data from (H) were analyzed and plotted. Each dot represents an individual data point.

(J) Association of myosin-II spot with γ-tubulin. Cells of the strain YCW0199 (*myp2-GFP alp4-TagRFP*) expressing Myp2-GFP and Alp4-TagRFP (γ-tubulin) and the strain YCW0201 [*GFP-myo2-myp2-(1,622–2104) alp4-TagRFP*] expressing Myo2-LT and Alp4-TagRFP were cultured to exponential phase in the EMM medium at 25°C and then subjected to microscopy. For YCW0199, cells were additionally cultured at 37°C for 2 h to induce the spot formation.

See also Figure S6.

both tail extensions, Myo2-ST (max: 42.4 ± 3.5%; $T_{1/2}$: 73.1 ± 17.1 s; n = 15) and Myo2-LT (max: 45.2 ± 3.5%; $T_{1/2}$: 103.0 ± 17.7 s; n = 19), converted Myo2 from a mobile to an immobile state, as manifested by the increased $T_{1/2}$ values (Figures 4B, 4C, and S4, and Video S5). Myo2-LT recovered more slowly than Myo2-ST, indicating that the immobility of chimeras was dependent on the length of the Myp2-tail extension. The absence of Myp2 did not alter the immobility of chimeras, ruling out the possibility that the immobility was caused by an interaction with the endogenous Myp2 (Figures S6A, S6B, and S4). Together, these data suggest that the second CC region of Myp2 is largely responsible for its immobility during cytokinesis.

To further characterize the chimera alleles, we followed the behaviors of the chimeras throughout the cell cycle by time-lapse microscopy. At the time of spindle formation, unlike the WT (Figure 1A), neither chimera displayed robust node formation (Figures 4D and 4E, −30 min), as reflected by the dampened first peak in the accumulation kinetics (Figure 4F). This result suggests either that a high turnover rate of Myo2 is required for efficient node formation or that the chimeras may compromise their interactions with the "node organizer" Mid1, an anillin-like protein in fission yeast (Motegi et al., 2004; Wu et al., 2006). Despite the decrease in node formation, cells carrying the chimera alleles were able to form an intact ring that constricted with a comparable rate as the WT Myo2 did (Figure 4G and Table S1). Surprisingly, GFP-Myo2-LT formed bright "spots" at 25°C, which localized to the cell equator and merged into a ring structure (Figure 4E). During ring constriction, Myo2-LT disassembled as spots, which moved away from the division site. The Myo2-LT spots are similar to the Myp2-GFP "spots" that were observed when cells were grown at 37°C (Figure 4H) (Wu et al., 2006). At the high temperature, a majority of the *myp2*$^{+}$*-GFP* formed bright spots, whereas very few cells formed weak spots at 25°C (Figures 4H and 4I). Interestingly, the spots were largely abolished in the *myp2* truncation mutants, especially in the *myp2-(1,621)-GFP* mutant in which only 5% of the cells contained spots at 37°C whose intensities were significantly lower than those of the Myp2-GFP spots at 37°C (Figures 4H and 4I). On the other hand, a majority of the cells carrying either chimera allele formed robust spots at 37°C (77% for *myo2-ST* and 100% for *myo2-LT*) whose intensities were significantly higher than those of the GFP-Myo2 spots at 37°C (Figures 4H and 4I). A deletion of *myp2*$^{+}$ did not reduce the efficiency of spot formation for the chimera alleles (71% for *myo2-ST myp2*Δ and 100% for *myo2-LT myp2*Δ) (Figures 4H and 4I). Together, these data indicate that the second CC region of Myp2 is essential for its spot formation at the high temperature and the same region of Myp2 is sufficient to confer Myo2 the ability to form spots independently of Myp2.

The apparent association of the GFP-Myo2-LT spots with the microtubules (Figure 4E) and the known interaction between Myp2 and Mto1, an activator of the γ-tubulin complex (Samejima et al., 2010), raised the possibility that the spots might be associated with the γ-tubulin complex. To test this possibility, we performed dual-color imaging of cells expressing the γ-tubulin complex subunit Alp4-TagRFP in combination with Myp2-GFP or GFP-Myo2-LT. As expected, some of the Myp2-GFP and GFP-Myo2-LT spots co-localized with Alp4-TagRFP (Figure 4J). This result suggests that the second CC region may mediate the interaction between Myp2 and Mto1.

Despite acquiring some Myp2-like features by the chimeras, neither chimera (*myo2-ST* or *myo2-LT*) was able to suppress the KCl sensitivity of *myp2Δ* cells at 18 or 25°C (Figure S6C). This is consistent with the observation that the ST or LT is dispensable for the protective role of Myp2 against high-salt stress (Figure 3F). The Myo2-LT also failed to suppress the accumulation and constriction defects of Myo2 caused by *myp2Δ* (Figures S6D and S6E). These data indicate that the second CC region is necessary but not sufficient for the contribution of Myp2 to the overall rate of ring constriction.

Collectively, these data suggest that the second CC region of Myp2 is critical for its immobile behavior during cytokinesis and likely mediates its interaction with Mto1 to control PAA formation at the division site.

Myo2 and Myp2 Are Differentially Required for Contractile Ring Assembly and Constriction as well as for Guiding Bgs1 Localization and PS Formation during Cytokinesis

Myo2 and Myp2 are required for cytokinesis under normal and stressed conditions, respectively (Kitayama et al., 1997; Bezanilla et al., 1997; Motegi et al., 2000; Laplante et al., 2015; Palani et al., 2017). PS formation, i.e., the synthesis of 1,3-β-D-glucan at the division site by the β-glucan synthase Bgs1/Cps1 (hereafter Bgs1), is also essential for cytokinesis (Liu et al., 1999; Cortes et al., 2002, 2007). Importantly, the primary force for furrow ingression is provided by PS formation rather than by AMR constriction (Proctor et al., 2012). However, the relationship between the AMR and PS formation remains unclear. In *S. cerevisiae*, the AMR is thought to guide PS formation during cytokinesis in addition to force production (Vallen et al., 2000; Bi, 2001; Schmidt et al., 2002; Lord et al., 2005; Fang et al., 2010). To determine whether this concept applies to fission yeast, we performed 3D time-lapse microscopy to monitor the spatiotemporal dynamics of AMR assembly and constriction (marked by Rlc1-tdTomato), GFP-Bgs1 accumulation at the division site, and PS formation (Calcofluor White [CW] staining) in WT cells as well as cells carrying *myo2-E1*, *myp2Δ*, or *myo2-E1 myp2Δ* at both the permissive (25°C) and non-permissive (36°C) temperatures for the *myo2-E1* allele (Balasubramanian et al., 1998). A unique strength of this experiment is that the spatiotemporal relationship between the AMR, the accumulation of the "cargo" enzyme, Bgs1, at the division site, and the activation of Bgs1, as manifested by PS formation, can be directly visualized in real time and determined quantitatively at the single-cell level.

At 25°C, Rlc1 in WT cells behaved as expected (Figures 5A and S7A, and Video S6). It first formed nodes near the cell equator and then coalesced into a ring, which then constricted to a dot, followed by disappearance. The time span from the first appearance of a ring-like structure to its disappearance was ~33 min (Figures 5A and 5F). Bgs1 began to accumulate at the division site ~7.5 min before the first appearance of a Rlc1 ring without any individual nodes nearby and lasted at the division site for ~90 min (Figure 5A). CW staining was first detected at the division site ~10 min after the initial localization of Bgs1, and this signal retained at the division site about ~60 min (Figure 5A). The disappearance of CW staining presumably indicates the degradation of the PS, which enables cell separation. Thus, AMR formation, Bgs1 accumulation, PS formation (an indicator of Bgs1 activation), and cell separation follow strict temporal order and display distinct kinetics (Figures 5A and S7E).

The temporal order of and the interval between these cellular events were preserved in *myp2Δ* cells (Figures 5A and S7B, and Video S6). However, the duration for each molecule, structure, or process was prolonged (Rlc1 ring: ~40 min; Bgs1 localization: ~100 min; PS: ~85 min) as indicated by the altered kinetics of accumulation and removal of Rlc1, Bgs1, and CW signals at the division site (Figures 5A and S7E). In *myo2-E1* cells, Bgs1 highly accumulated (>85% of the peak) at the division site before the formation of a smooth-looking Rlc1 ring (Figures 5A and S7C, and Video S6). This change likely reflects the mild deficiency of the mutant cells in AMR assembly at the permissive temperature (Palani et al., 2017). These data, together with those described earlier for WT and *myp2Δ* cells, indicate that the timing for the initial AMR assembly is dictated solely by Myo2, not Myp2. PS formation was also slightly and variably delayed in *myo2-E1* cells in relation to the initial localization of Bgs1 at the division site (Bgs1→PS: ~15 min). As the product of *myo2-E1* lacks motor activity at a wider range of temperature (4–42°C) (Stark et al., 2013) and is defective in actin-filament binding *in vitro* (Lord and Pollard, 2004), this result suggests that the motor activity of Myo2 is not essential for PS formation. Similar to *myp2Δ* cells, the duration for the Rlc1 ring (~60 min), Bgs1 (~115 min), and PS formation (~110 min) at the division site was prolonged (Figures 5A and S7E). Thus, both Myo2 and Myp2 contribute to AMR maturation and/or constriction, and both affect the subsequent Bgs1 accumulation and PS formation at the division site. In the *myo2-E1 myp2Δ* double mutant, the initial localization of Bgs1 to the division site occurred before the formation of a smooth Rlc1 ring, similar to the *myo2-E1* single mutant (Figure S7D, and Video S6). The PS formation in relation to Bgs1 localization at the division site (Bgs1→PS: ~15 min) was unchanged from that of the single mutant. This further emphasizes that the collective motor activity of Myo2 and Myp2 is dispensable for Bgs1 activation or PS formation. The Rlc1 ring (~90 min), Bgs1 localization (>135 min), and CW signal (>120 min) were all retained at the division site for a longer time in the double mutant than in WT or the single mutants (Figures 5A and S7E). Most strikingly, the CW signal never disappeared completely in the double mutant.

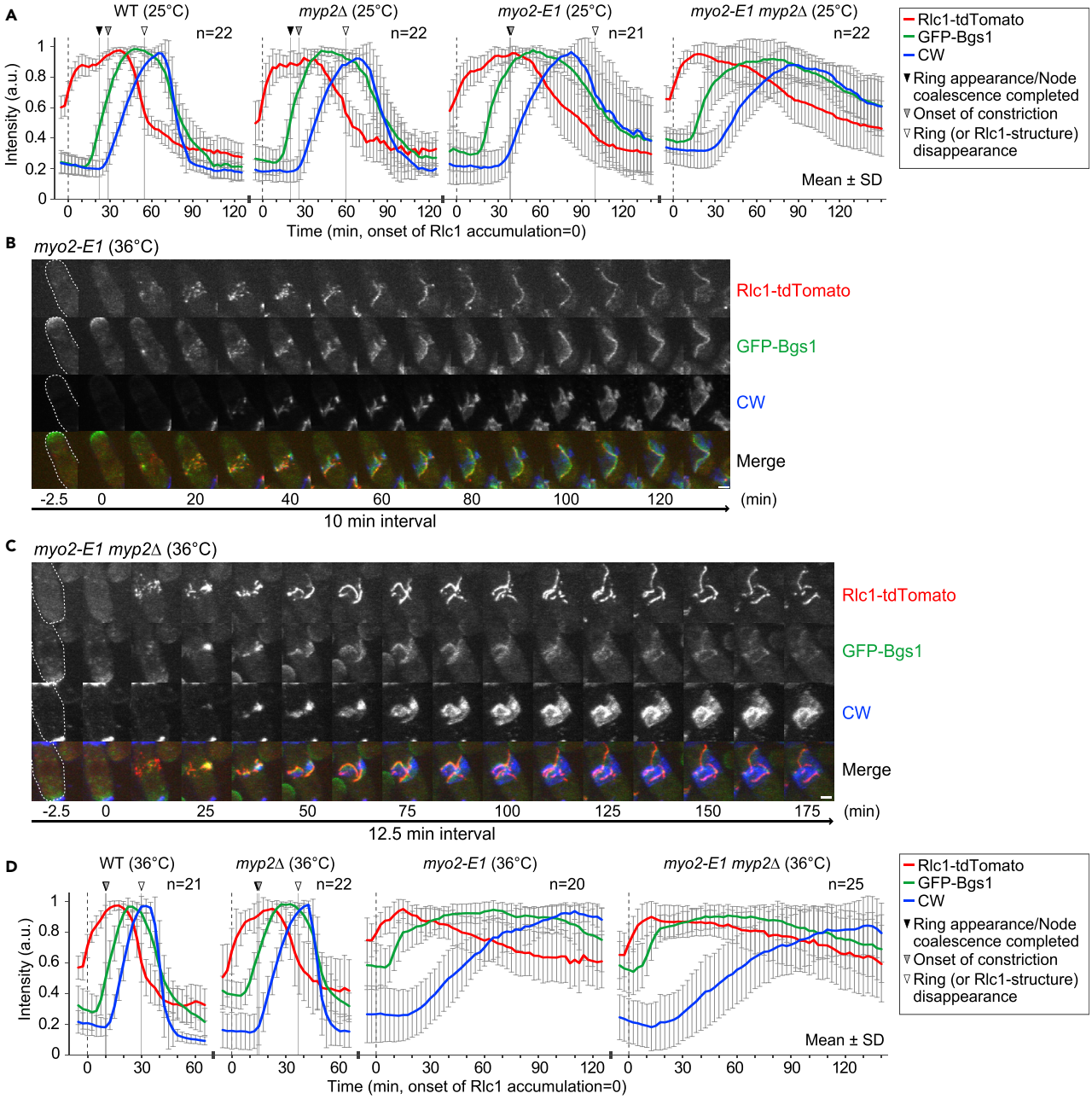

F

Temp.	Genotype	Time (min, onset of Rlc1 accumulation=0) ▼Ring appearance	▽Onset of constriction	▽Ring disappearance
25°C	WT	22.3 ± 3.2	28.6 ± 2.8	54.8 ± 2.4
	myp2Δ	20.3 ± 3.0	26.4 ± 3.1	60.0 ± 4.1
	myo2-E1	38.1 ± 4.7	38.3 ± 4.3	99.2 ± 29.1
	myo2-E1 myp2Δ	n/a	n/a	n/a
36°C	WT	10.1 ± 3.2	10.5 ± 2.6	30.0 ± 3.1
	myp2Δ	14.3 ± 2.5	15.0 ± 3.0	37.0 ± 3.7
	myo2-E1	n/a	n/a	n/a
	myo2-E1 myp2Δ	n/a	n/a	n/a

Figure 5. Myo2 and Myp2 Are Collectively Essential for AMR Assembly and Constriction as well as for Bgs1-Mediated PS Formation

(A) Kinetics of AMR formation, Bgs1 cargo accumulation, and PS formation at 25°C. AMR formation (Rlc1-tdTomato), Bgs1 accumulation, and PS formation were visualized by time-lapse analysis of cells of WT (YCW0117: *GFP-bgs1 rlc1-tdTomato*), *myp2*Δ (YCW0043: *myp2*Δ *GFP-bgs1 rlc1-tdTomato*), *myo2-E1* (YCW0044: *myo2-E1 GFP-bgs1 rlc1-tdTomato*), and *myo2-E1 myp2*Δ (YCW0047: *myo2-E1 myp2*Δ *GFP-bgs1 rlc1-tdTomato*) strains at 25°C or 36°C. To visualize PS, CW (50 μg/mL) was supplemented to the medium during imaging. See also Figures S7 and S8, and Video S6.

(B and C) Myo2 and Myp2 are required not only for ring assembly and constriction but also for guiding Bgs1 deposition and PS formation. Montages are created from representative cells of the strains YCW0044 (B) and YCW0047 (C) imaged in (A). See also Video S6. Scale bar, 2 μm.

(D) Kinetics of AMR formation, Bgs1 cargo accumulation, and PS formation at 36°C. The same strains as in (A) were imaged at 36°C. See also Figure S8.

(E) Distinct and shared roles of Myo2 and Myp2 in cytokinesis. AMR constriction of imaging data from panels A and D were analyzed. Cells were quantified based on three categories of phenotypes: (1) completed (symmetric ring constriction), (2) completed (asymmetric and/or skewed ring constriction), or (3) failed (no ring constriction and/or no membrane closure during the imaging period).

(F) Timing of AMR assembly, constriction, and disassembly in WT and different myosin-II mutants. Timing of the ring appearance (black arrowhead), onset of the ring constriction (gray arrowhead), and the ring disappearance (white arrowhead) was measured from imaging analysis in panels A and D. "n/a" indicates "not analyzed" owing to lack of the ring assembly in the mutants.

Thus, Myo2 and Myp2 play a synergistic role in AMR maturation and constriction, Bgs1 localization, and PS formation at 25°C, and defects in these processes presumably affect PS degradation.

At 36°C, in WT cells, the coalescence of Rlc1 nodes into a ring occurred simultaneously with the initial localization of Bgs1 to the division site, which was followed ~2.5 min later by PS formation (Figures 5D and S8A, and Video S6). The durations of the Rlc1 ring (~20 min), Bgs1 localization (~45 min), and PS formation (~40 min) at the division site were all shortened in comparison with those of WT cells at 25°C (Figures 5D, 5F, and S8C). In *myp2Δ* cells, the temporal order for the first appearance of Rlc1 ring, Bgs1 localization, and PS formation were indistinguishable from those in WT cells (Figures 5D, S8B, and S8C). However, the duration for each molecule, structure, or process was slightly prolonged (Rlc1 ring: ~23 min; Bgs1 localization: ~50 min; PS: ~45 min), suggesting that Myp2 plays a relatively minor role in cytokinesis at 36°C. In *myo2-E1* cells, when Bgs1 first appeared as puncta at the division site, Rlc1 still existed in nodes (Figure 5B and Video S6). The Bgs1 puncta appeared to associate with some of the Rlc1 nodes. These nodes were gradually "transformed" into cable-like structures (in 30–40 min from the initial Bgs1 localization). This transition most likely corresponds to the timing of Rlc1 ring assembly in WT cells. The Bgs1 localization was followed ~15 min later by PS formation (Figures 5B and 5D, and Video S6). Strikingly, as the Rlc1 cables grew away from the midpoint of the cell, these cables were followed closely by Bgs1 localization and the synthesis of septal materials (Figures 5B and Video S6). The resolution at which the spatial relationship between the cytokinesis events was visualized in the mutant would be difficult to achieve in WT cells, as all cytokinesis proteins are highly concentrated in a narrow region at the division site in WT cells. These data strongly suggest that the Rlc1 cables act as a "compass" that guides Bgs1 deposition and PS formation during cytokinesis. We hypothesize that this guiding role requires the formation of a cytoskeletal structure such as the AMR in WT cells or its fragments such as the Rlc1 cables as described earlier. At the molecular level, such a guiding role could be achieved via a direct interaction between myosin-II and Bgs1, which has not been reported. Alternatively, it could involve linker proteins such as Sbg1 that physically interacts with Bgs1 and the ring components, including the F-BAR proteins (Imp2 and Cdc15) and the paxillin-like protein Pxl1 (Sethi et al., 2016; Davidson et al., 2016). Similarly, in budding yeast, the F-BAR protein Hof1 links the AMR to PS formation by interacting with the tail of myosin-II (Myo1) and Chs2, the chitin synthase-II, a secretory cargo that is essential for PS formation (Oh et al., 2013). Equally strikingly, the Rlc1 cables, Bgs1 localization, and the PS never completely disappeared from the division site during the imaging period (2 h or longer) (Figures 5B and 5D, and Video S6). This result suggests that the motor activity of Myo2 (assuming that the *myo2-E1* product is folded properly at 36°C) is required for AMR disassembly and Bgs1 removal, and defects in these processes affect septum degradation. The *myo2-E1 myp2Δ* double mutant behaved similarly to the *myo2-E1* cells at 36°C (Figures 5C–5E), again highlighting a minor role of Myp2 in cytokinesis at 36°C.

Taken together, these data indicate that Myo2 and Myp2 play distinct and shared roles in AMR assembly and constriction as well as in guiding Bgs1 localization and PS formation during cytokinesis.

Myo2, Myp2, and Actin Filaments Are Differentially Required for the Spatial Distribution but Not Activation of Bgs1 at the Division Site during Cytokinesis

The genetic and cell biological experiments described in Figure 5 all suggest that Myp2 plays little or no obvious role in cytokinesis at 36°C. However, because all cellular events of cytokinesis including AMR

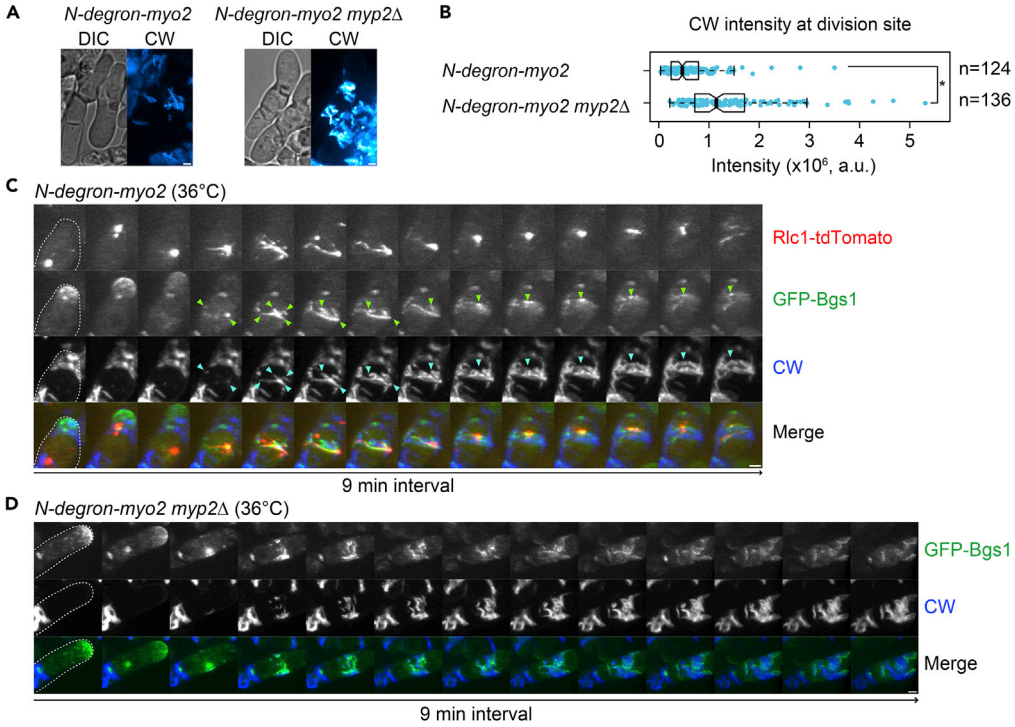

Figure 6. Myo2 and Myp2 Play Distinct Roles in Guiding Bgs1 Deposition and PS Formation

(A) PS formation in the absence of Myo2 and Myp2. Strains of *N-degron-myo2* (YCW0046: *N-degron-myo2 GFP-bgs1 rlc1-tdTomato*) and *N-degron-myo2 myp2Δ* (YCW0045: *N-degron-myo2 myp2Δ GFP-bgs1*) were used for analysis. To induce Myo2 degradation, cells were cultured in YE5S at 36°C for 12 h and then stained by CW (50 μg/mL).

(B) Increased deposition of septal materials in myosin-II-depleted cells. Imaging data from (A) were analyzed. Each dot represents an individual data point. The box covers the region from the first quartile to the third quartile. The bold line and the notch of the box represent the median and 95% confidence interval of the median, respectively. The whiskers at either side of the box extend to 1.5 interquartile ranges from the quartiles. * = $p < 0.01$ by Student's t test.

(C and D) Myo2 and Myp2 are differentially required for guiding PS formation at division site. Strains of *N-degron-myo2* (YCW0046) (C) and *N-degron-myo2 myp2Δ* (YCW0045) (D) were used for time-lapse analysis. Cells were cultured in YE5S at 36°C for 6 h to deplete Myo2 before imaging.

See also Video S7. Scale bar, 2 μm.

assembly, constriction, disassembly, and PS formation and degradation occurred much more quickly at 36°C than at 25°C, and because in all strains WT Myo2 or its motor activity-deficient mutant (*myo2-E1*) was present, it remains possible that a fine-tuning function of Myp2 in cytokinesis was masked by the presence of Myo2 at 36°C. To test this possibility, we conditionally degraded Myo2 (*N-degron-myo2*) at 36°C in *myp2*$^{+}$ and *myp2Δ* cells and monitored the depletion impact on AMR assembly, Bgs1 localization, PS formation, and their disassembly or removal processes. After incubating cells at 36°C for 6 h, no cells were found to form Rlc1 nodes, indicative of Myo2 depletion, which is consistent with a previous report (Laporte et al., 2011). Strikingly, PS formation was much more defective, with aberrant morphology and increased glucan deposition, in the absence of Myp2 than in its presence (Figures 6A and 6B), indicating a clear role of Myp2 in PS formation during cytokinesis at 36°C.

Time-lapse analysis showed that, when Myo2 was depleted in otherwise WT background (Figure 6C and Video S7), Rlc1 could not form a ring-like structure; instead, it localized to the division site as a mixture of cables and patches. Bgs1 also localized to the division site in the form of cables and patches, a majority of which co-localized with Rlc1. Over time, their co-localization became less obvious, which could be caused by the dynamic change in Rlc1 and Bgs1 organization. PS formation began ~3 min after the initial localization of Bgs1 and strictly followed the pattern of Bgs1 localization (Figure 6C, arrowhead). Rlc1, Bgs1, and CW signals were retained at the division site at the end of the imaging period, i.e., 105 min after the initial localization of Bgs1. These data suggest that Myo2 plays a major role in AMR assembly as well as in guiding Bgs1 deposition and PS formation at 36°C.

To determine the role of Myp2 in the division process under the same condition as described earlier, we depleted Myo2 in *myp2Δ* cells and found that Bgs1 was still delivered to the division site (Figure 6D and Video S7). This is not surprising, as the polarized transport system for Bgs1 is presumably intact. However, Bgs1 was present as a cloud of "puncta" spanning a wide region near cell equator (~2–8 μm) instead of a sharp ring-like structure. These data suggest that Myo2 and Myp2 are collectively essential for guiding the deposition of Bgs1 at the division site. These Bgs1 puncta initiated the synthesis of septal materials shortly after their arrival (usual in 3 min). The interval between the initial localization of Bgs1 and its activation is similar to that of WT cells (~2.5 min) (Figures 6D and S8A), indicating that Bgs1 can be efficiently activated independently of myosin-II. The Bgs1 puncta later became cable-like structures oriented toward different directions. Strikingly, these puncta and cables always co-localized with CW signals, suggesting that the enzyme Bgs1 can anchor to its product (the 1,3-β-D-glucan polymer) and/or its substrate during glucan synthesis in the absence of the myosin guide. In budding yeast, it was observed that a chitin synthase and an 1,3-β-D-glucan synthase could be trapped by their respective insoluble products *in vitro*, and this observation was used to enrich and purify the synthase (Kang et al., 1984; Inoue et al., 1995). Based on these observations and the PS phenotype of *myp2Δ* cells described earlier, we conclude that Myo2 and Myp2 are differentially required and collectively essential for the deposition, but not activation, of Bgs1 at the division site.

To determine the role of actin filaments in the contractile ring in Bgs1 deposition and PS formation, we performed time-lapse microscopy on a mixture of cells carrying LifeAct-GFP and Rlc1-tdTomato (Figure 7A and Video S8) and those carrying GFP-Bgs1 and Rlc1-tdTomato (Figures 7B and 7C, and Video S8) in the presence of 0.5 and 1 μM Latrunculin A (LatA) at 25°C. Under these conditions, actin cables were undetectable, but actin "patches" remained. Rlc1 initially localized to the division site as nodes. About 18–21 min later, those nodes coalesced into several cables oriented toward different directions. The cables could further coalesce or flow away from the division site. Individual Rlc1 cables invariably co-localized with Bgs1 (Figure 7B) and CW signals (Figures 7A and 7B) often at several locations, leading to the fragmented appearance of the PS in individual cells. The Rlc1 cables were always associated with a few actin patches along their lengths (Figure 7A). Thus, it is unclear whether myosin, actin filaments, or both are required for guiding PS formation. To this end, we noted that actin patches free of Rlc1 never co-localized with CW signals regardless of location and cell-cycle time (Figure 7A), suggesting that actin filaments on their own cannot guide PS formation. Interestingly, the Rlc1 cables broke into pieces ~30 min after their formation, but these pieces were still able to retain and activate Bgs1 for PS formation (Figure 7B, and Video S8). Similarly, the Rlc1 nodes, which never coalesced into a ring structure, were able to recruit and activate Bgs1 (Figure 7C, and Video S8). We also imaged the same mixture of strains in the presence of 100 μM LatA at 25°C. Under this condition, actin cables and patches were abolished (Figure 7D) and weak Rlc1 puncta were observed (Figure 7E). Myp2 should not localize to the division site, as its localization depends on actin filaments (Wu et al., 2003). Surprisingly, each Rlc1 punctum was able to capture and activate Bgs1 in the absence of the actin cable-mediated transport system (Figure 7E, and Video S8), suggesting that myosin-II can either directly or indirectly guide PS formation in the absence of actin filaments.

To test this idea further, we monitored Bgs1 deposition and/or PS formation in cells with pre-formed AMRs at different constriction stages in the presence of 100 μM LatA. Previous work suggests that actin filaments are dispensable for cytokinesis, once the septation has started (Proctor et al., 2012). Consistent with this finding, we observed that PS formation that had progressed ~65% of the diameter of the division site was able to finish cytokinesis in the absence of actin filaments (Figure S9A). In these cells, an Rlc1 ring constriction was closely followed by Bgs1 localization and PS formation (Figures S9B and S3C). As Myp2 cannot be maintained at the division site in the presence of LatA (Wu et al., 2003), this result suggests that Myo2 can guide Bgs1 deposition and PS formation either directly or indirectly independent of actin filaments. In contrast, an Rlc1 ring at the early stage of constriction could not be maintained at the division site in the absence of actin filaments. Consequently, the cell failed to complete PS formation and cytokinesis (Figures S9D and S9E). Together, these data suggest that the concentration of myosin-II at the division site might be critical for guiding Bgs1 deposition and PS formation and that actin filaments play a supportive role by maintaining the myosin-II concentration at the division site, especially during early stage of constriction. This conclusion is supported by the observation that the accumulation of both myosin-II isoforms, especially Myp2, peaks in the middle of ring constriction (Figures 1C, 1D, and S5A).

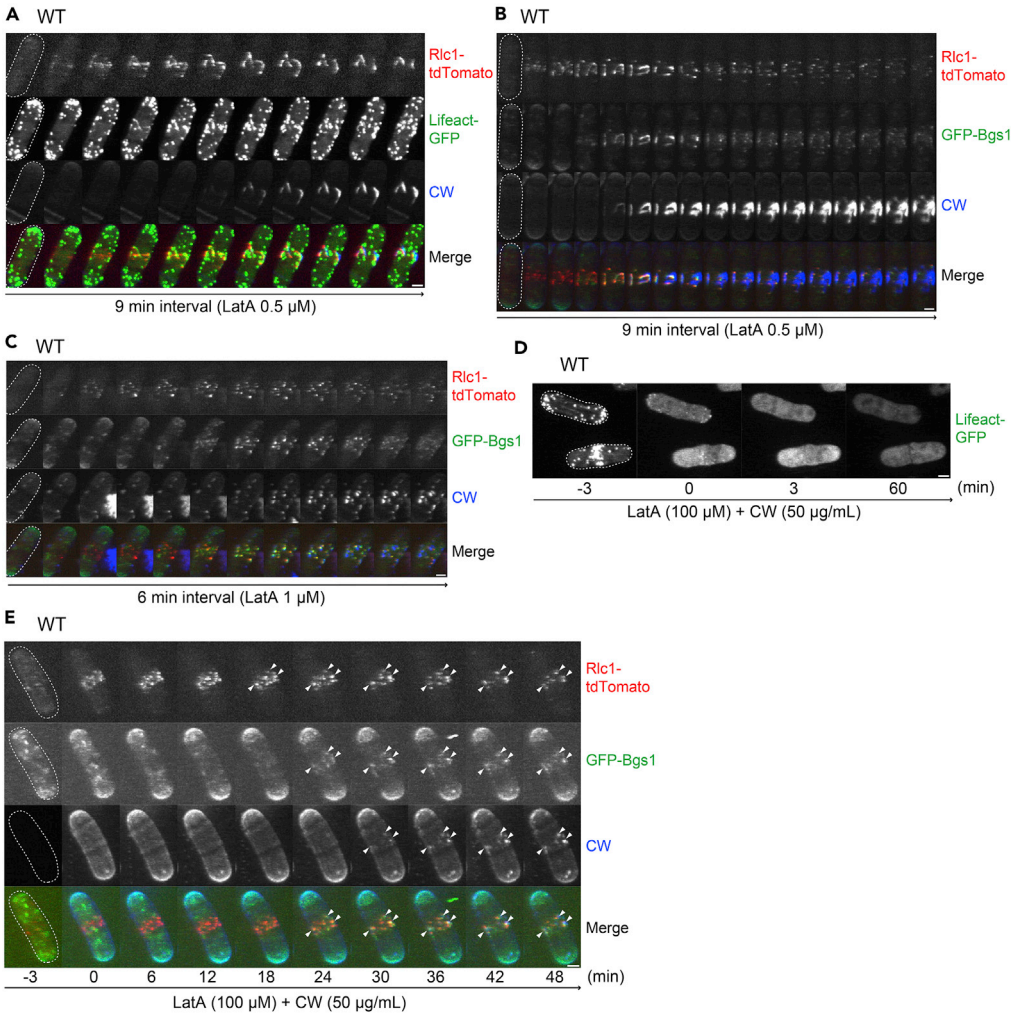

Figure 7. Actin Filaments Affect Bgs1 Deposition and PS Formation by Establishing and Maintaining Myosin-II Concentration and Architecture

(A–C) Actin filaments affect PS formation by promoting AMR assembly. Effects of low doses of LatA (0.5 and 1 μM) on AMR assembly, Bgs1 localization, and PS formation were determined by imaging a mixed culture of two WT strains (YCW0079: *GFP-lifeact rlc1-tdTomato*, and YCW0117). (A) YCW0079 (0.5 μM LatA), (B) YCW0117 (0.5 μM LatA), and YCW0117 (1 μM LatA). See also Video S8. Scale bar, 2 μm.

(D and E) Actin filaments are dispensable for Bgs1 recruitment and activation. The same experimental condition of (A–C) was used for imaging except in the presence of a higher LatA concentration (100 μM). (D) YCW0079 (100 μM LatA), and (E) YCW0117 (100 μM LatA).

See also Figure S9 and Video S8. Scale bar, 2 μm.

Despite the distinguishable roles for myosin and actin filaments in the process, our data indicate that only when the myosin and actin filaments are organized into a ring structure, the latter becomes a highly efficient and precision guide for Bgs1 deposition and PS formation.

DISCUSSION

In addressing the question of why more than one myosin-II isoform is expressed in a single cell to drive cytokinesis, we confirmed and extended previous observations that the myosin-II isoforms Myo2 and Myp2 in fission yeast display distinct localization patterns during the cell cycle, and that Myo2 is highly dynamic while Myp2 is immobile during cytokinesis (Pelham and Chang, 2002; Wloka et al., 2013; Takaine et al., 2015; Laplante et al., 2015; Palani et al., 2017). We also found that the initial assembly of the AMR is dictated by Myo2, but its rate of constriction is contributed by both Myo2 (for approximately two-thirds of

the rate) and Myp2 (approximately one-third). Importantly, we found that Myp2 controls the onset of Myo2 constriction, especially under high-salt stress (e.g., 0.6 M KCl). Further analysis has indicated that the second CC region in the Myp2 tail is required for its immobility during cytokinesis, its contribution to the rate of constriction, and its ability to form γ-tubulin-associated "spots" at the high temperature. Other regions of Myp2, such as the motor domain, determine its localization kinetics at the division site (Takaine et al., 2015) and is essential for its protective role in cell survival against high-salt stress at low temperatures. Similarly, a C-terminal region of Myo1, the sole myosin-II in budding yeast, is also required for its immobility and constriction (Wloka et al., 2013), whereas other regions of Myo1 tail are responsible for its localization to the division site (Fang et al., 2010). Thus, the basic behaviors between the slow-turnover myosin-IIs, Myp2 in fission yeast, and Myo1 in budding yeast during cytokinesis are conserved, despite their divergence over ~420 million years ago (Sipiczki, 2000). We also found that the non-muscle myosin-IIA displayed a higher turnover rate than IIB or IIC during cytokinesis in mammalian cells (Wang et al., 2019). A common theme begins to emerge: in systems harboring only one non-muscle myosin-II (such as budding yeast and *Drosophila*), the myosin is immobile during cytokinesis (Uehara et al., 2010; Wloka et al., 2013), whereas in systems harboring more than one myosin-II isoform (fission yeast and humans), some isoforms are immobile, whereas the others are dynamic during cytokinesis. It is worth noting that all the immobile myosin-IIs have longer tails than the dynamic ones. Strikingly, addition of the second CC region of Myp2 to Myo2 makes the latter less dynamic. Thus, it is tempting to speculate that the ancient myosin-II was immobile, which gave rise to a dynamic isoform through gene duplication, mutation, and truncation. Multiple isoforms with common and differential properties are expressed in a single cell to enable the robustness of cytokinesis under different growth conditions.

Indeed, Myo2 and Myp2 display distinct, yet interconnected, responses to cellular stresses. Under high osmolarity (such as 2 M sorbitol), both Myo2 and Myp2 undergo a stereotypical process of disassembly (stress response), reassembly (recovery), and constriction (adaptation). However, under high-salt stress (e.g., 1 M KCl), Myo2 still displays a similar response but Myp2 disassembles without subsequent recovery. Under this condition, Myp2 is essential for the timely disassembly of Myo2. Under moderate salt stress (e.g., 0.6 M KCl), Myp2 is required for the timely initiation of Myo2 constriction. These regulatory roles of Myp2 on Myo2 presumably explain why *myp2Δ* cells are inviable under high-salt stress. Thus, the interplay between different Myo2 and Myp2, despite the lack of mechanism at the moment, highlights the importance of the collective power of different myosin-II isoforms in endowing cytokinesis with robustness to buffer against environmental insults.

In addressing the question of whether the sole function of the AMR is to produce a contractile force that drives furrow ingression during cytokinesis, we monitored the kinetics of the AMR behavior, the deposition of the enzymatic cargo Bgs1 at the division site, and the synthesis of the PS at the single-cell level. This has led to a clear visualization of the spatiotemporal relationship between the AMR and PS synthesis in real time. Using this approach, we found that the AMR guides Bgs1 deposition and PS formation and this guiding role can occur independently of the myosin-II motor activity. Both Myo2 and Myp2 contribute to and are collectively essential for the guiding process. Actin filaments also make important, although indirect, contribution to the guiding process by organizing myosin-II into a ring structure and then stabilizing the ring structure and maintaining myosin-II concentration at the division site during early stage of constriction. Thus, the AMR in WT cells likely provides a structural scaffold (a motor-independent function) that dynamically adjusts its size (through motor-dependent constriction) to efficiently and precisely guide PS synthesis at the leading edge of an ingressing membrane during cytokinesis. PS formation, in turn, drives furrow ingression (Proctor et al., 2012). When the AMR guide is abolished, Bgs1 is still delivered to the middle portion of the cell and drives PS formation from multiple foci toward multiple directions. Thus, the role of the AMR is to guide, not to activate, Bgs1 for PS formation. Bgs1 activation is presumably carried out by a timed mechanism, such as Rho1 activation, during cytokinesis, as Rho1 is known to localize to the division site and regulate glucan synthesis in fission yeast (Arellano et al., 1996, 1997).

In budding yeast, the AMR and PS formation are interdependent (Bi, 2001; Schmidt et al., 2002). The AMR was proposed to guide septum formation (Vallen et al., 2000; Fang et al., 2010; Wloka et al., 2013), whereas the PS is thought to stabilize the AMR during its constriction (Bi, 2001; Schmidt et al., 2002; VerPlank and Li, 2005). The guiding role of the AMR is largely independent of myosin-II motor activity, as a "headless" AMR, which constricts at ~70%-80% of the normal rate (Lord et al., 2005; Fang et al., 2010), can guide PS formation with a mild defect in septal orientation (Fang et al., 2010). Within the AMR, myosin-II plays a more important role than actin filaments in guiding PS formation, as deletion

of *MYO1*, which abolishes the AMR (Bi et al., 1998) and deletion of the Calponin-Homology Domain (CHD) of Iqg1 (the sole IQGAP in budding yeast), which selectively disrupts the actin ring (Shannon and Li, 1999; Fang et al., 2010), resulted in major and minor defects in the orientation of the PS, respectively (Fang et al., 2010). Thus, the similarities between the budding yeast and fission yeast in terms of the AMR acting as a spatial guide for PS formation during cytokinesis are striking. Given that synthesis of a glycosaminoglycan (GAG), a common ECM component in animal cells and a functional counterpart of the PS in yeast cells, is required for embryonic cytokinesis in *C. elegans* and mice (Mizuguchi et al., 2003; Izumikawa et al., 2010), it would be of a great interest to determine whether the AMR also guides localized ECM remodeling during cytokinesis in animal cells.

Limitations of the Study

In this study, we have demonstrated clearly that the second CC region of Myp2 is required for its immobility during cytokinesis, and that Myp2 controls the timely disassembly, stability, and constriction initiation of the Myo2 ring during stress response. The molecular mechanisms underlying these newly defined roles of Myp2 in cytokinesis remain unknown. Further structure-function analysis of Myp2 using both *in vivo* and *in vitro* approaches is required for gaining the desired mechanistic insights.

METHODS

All methods can be found in the accompanying Transparent Methods supplemental file.

SUPPLEMENTAL INFORMATION

Supplemental Information can be found online at https://doi.org/10.1016/j.isci.2019.03.014.

ACKNOWLEDGMENTS

We thank Andrea Stout of the CDB Imaging Core for assistance, the members of Phong Tran laboratory for strains and reagents, and the members of Bi laboratory, especially Joey Marquardt, for discussions. This work was supported by a Ph.D. Fellowship from the Boehringer Ingelheim Fonds to C.W. and NIH grants GM115420 to E.B. and GM118746 to J.-Q.W.

AUTHOR CONTRIBUTIONS

Conceptualization, C.W., H.O., and E.B.; Methodology, C.W., H.O., J.-Q.W., and E.B.; Investigation, C.W., H.O., and J.-Q.W.; Writing, H.O. and E.B.; Supervision, E.B.

DECLARATION OF INTERESTS

The authors declare no competing interests.

Received: July 20, 2018
Revised: January 30, 2019
Accepted: March 12, 2019
Published: April 26, 2019

REFERENCES

Arellano, M., Duran, A., and Perez, P. (1996). Rho 1 GTPase activates the (1-3)beta-D-glucan synthase and is involved in *Schizosaccharomyces pombe* morphogenesis. EMBO J. *15*, 4584–4591.

Arellano, M., Duran, A., and Perez, P. (1997). Localisation of the *Schizosaccharomyces pombe* rho1p GTPase and its involvement in the organisation of the actin cytoskeleton. J. Cell Sci. *110*, 2547–2555.

Balasubramanian, M.K., Bi, E., and Glotzer, M. (2004). Comparative analysis of cytokinesis in budding yeast, fission yeast and animal cells. Curr. Biol. *14*, R806–R818.

Balasubramanian, M.K., Mccollum, D., Chang, L., Wong, K.C., Naqvi, N.I., He, X., Sazer, S., and Gould, K.L. (1998). Isolation and characterization of new fission yeast cytokinesis mutants. Genetics *149*, 1265–1275.

Bezanilla, M., Forsburg, S.L., and Pollard, T.D. (1997). Identification of a second myosin-II in *Schizosaccharomyces pombe*: myp2p is conditionally required for cytokinesis. Mol. Biol. Cell *8*, 2693–2705.

Bezanilla, M., and Pollard, T.D. (2000). Myosin-II tails confer unique functions in *Schizosaccharomyces pombe*: characterization of a novel myosin-II tail. Mol. Biol. Cell *11*, 79–91.

Bezanilla, M., Wilson, J.M., and Pollard, T.D. (2000). Fission yeast myosin-II isoforms assemble into contractile rings at distinct times during mitosis. Curr. Biol. *10*, 397–400.

Bhavsar-Jog, Y.P., and Bi, E. (2017). Mechanics and regulation of cytokinesis in budding yeast. Semin. Cell Dev. Biol. *66*, 107–118.

Bi, E. (2001). Cytokinesis in budding yeast: the relationship between actomyosin ring function and septum formation. Cell Struct. Funct. *26*, 529–537.

Bi, E., Maddox, P., Lew, D.J., Salmon, E.D., Mcmillan, J.N., Yeh, E., and Pringle, J.R. (1998). Involvement of an actomyosin contractile ring in

Saccharomyces cerevisiae cytokinesis. J. Cell Biol. *142*, 1301–1312.

Colman-Lerner, A., Chin, T.E., and Brent, R. (2001). Yeast Cbk1 and Mob2 activate daughter-specific genetic programs to induce asymmetric cell fates. Cell *107*, 739–750.

Cortes, J.C., Ishiguro, J., Duran, A., and Ribas, J.C. (2002). Localization of the (1,3)beta-D-glucan synthase catalytic subunit homologue Bgs1p/Cps1p from fission yeast suggests that it is involved in septation, polarized growth, mating, spore wall formation and spore germination. J. Cell Sci. *115*, 4081–4096.

Cortes, J.C., Konomi, M., Martins, I.M., Munoz, J., Moreno, M.B., Osumi, M., Duran, A., and Ribas, J.C. (2007). The (1,3)beta-D-glucan synthase subunit Bgs1p is responsible for the fission yeast primary septum formation. Mol. Microbiol. *65*, 201–217.

D'Souza, V.M., Naqvi, N.I., Wang, H., and Balasubramanian, M.K. (2001). Interactions of Cdc4p, a myosin light chain, with IQ-domain containing proteins in *Schizosaccharomyces pombe*. Cell Struct. Funct. *26*, 555–565.

Davidson, R., Pontasch, J.A., and Wu, J.Q. (2016). Sbg1 is a novel regulator for the localization of the beta-glucan synthase Bgs1 in fission yeast. PLoS One *11*, e0167043.

Ding, D.Q., Chikashige, Y., Haraguchi, T., and Hiraoka, Y. (1998). Oscillatory nuclear movement in fission yeast meiotic prophase is driven by astral microtubules, as revealed by continuous observation of chromosomes and microtubules in living cells. J. Cell Sci. *111* (Pt 6), 701–712.

Dobbelaere, J., and Barral, Y. (2004). Spatial coordination of cytokinetic events by compartmentalization of the cell cortex. Science *305*, 393–396.

Fang, X., Luo, J., Nishihama, R., Wloka, C., Dravis, C., Travaglia, M., Iwase, M., Vallen, E.A., and Bi, E. (2010). Biphasic targeting and cleavage furrow ingression directed by the tail of a myosin-II. J. Cell Biol. *191*, 1333–1350.

Feng, Z., Okada, S., Cai, G., Zhou, B., and Bi, E. (2015). MyosinII heavy chain and formin mediate the targeting of myosin essential light chain to the division site before and during cytokinesis. Mol. Biol. Cell *26*, 1211–1224.

Inoue, S.B., Takewaki, N., Takasuka, T., Mio, T., Adachi, M., Fujii, Y., Miyamoto, C., Arisawa, M., Furuichi, Y., and Watanabe, T. (1995). Characterization and gene cloning of 1,3-beta-D-glucan synthase from *Saccharomyces cerevisiae*. Eur. J. Biochem. *231*, 845–854.

Izumikawa, T., Kanagawa, N., Watamoto, Y., Okada, M., Saeki, M., Sakano, M., Sugahara, K., Sugihara, K., Asano, M., and Kitagawa, H. (2010). Impairment of embryonic cell division and glycosaminoglycan biosynthesis in glucuronyltransferase-I-deficient mice. J. Biol. Chem. *285*, 12190–12196.

Kang, M.S., Elango, N., Mattia, E., Au-Young, J., Robbins, P.W., and Cabib, E. (1984). Isolation of chitin synthetase from *Saccharomyces cerevisiae*. Purification of an enzyme by entrapment in the reaction product. J. Biol. Chem. *259*, 14966–14972.

Kitayama, C., Sugimoto, A., and Yamamoto, M. (1997). Type II myosin heavy chain encoded by the *myo2* gene composes the contractile ring during cytokinesis in *Schizosaccharomyces pombe*. J.Cell Biol. *137*, 1309–1319.

Kondo, T., Hamao, K., Kamijo, K., Kimura, H., Morita, M., Takahashi, M., and Hosoya, H. (2011). Enhancement of myosin II/actin turnover at the contractile ring induces slower furrowing in dividing HeLa cells. Biochem. J. *435*, 569–576.

Laplante, C., Berro, J., Karatekin, E., Hernandez-Leyva, A., Lee, R., and Pollard, T.D. (2015). Three myosins contribute uniquely to the assembly and constriction of the fission yeast cytokinetic contractile ring. Curr. Biol. *25*, 1955–1965.

Laporte, D., Coffman, V.C., Lee, I.J., and Wu, J.Q. (2011). Assembly and architecture of precursor nodes during fission yeast cytokinesis. J. Cell Biol. *192*, 1005–1021.

Liu, J., Wang, H., Mccollum, D., and Balasubramanian, M.K. (1999). Drc1p/Cps1p, a 1,3-beta-glucan synthase subunit, is essential for division septum assembly in *Schizosaccharomyces pombe*. Genetics *153*, 1193–1203.

Lord, M., Laves, E., and Pollard, T.D. (2005). Cytokinesis depends on the motor domains of myosin-II in fission yeast but not in budding yeast. Mol. Biol. Cell *16*, 5346–5355.

Lord, M., and Pollard, T.D. (2004). UCS protein Rng3p activates actin filament gliding by fission yeast myosin-II. J. Cell Biol. *167*, 315–325.

McDonald, N.A., Lind, A.L., Smith, S.E., Li, R., and Gould, K.L. (2017). Nanoscale architecture of the *Schizosaccharomyces pombe* contractile ring. Elife *6*, https://doi.org/10.7554/eLife.28865.

Mizuguchi, S., Uyama, T., Kitagawa, H., Nomura, K.H., Dejima, K., Gengyo-Ando, K., Mitani, S., Sugahara, K., and Nomura, K. (2003). Chondroitin proteoglycans are involved in cell division of *Caenorhabditis elegans*. Nature *423*, 443–448.

Motegi, F., Mishra, M., Balasubramanian, M.K., and Mabuchi, I. (2004). Myosin-II reorganization during mitosis is controlled temporally by its dephosphorylation and spatially by Mid1 in fission yeast. J. Cell Biol. *165*, 685–695.

Motegi, F., Nakano, K., Kitayama, C., Yamamoto, M., and Mabuchi, I. (1997). Identification of Myo3, a second type-II myosin heavy chain in the fission yeast *Schizosaccharomyces pombe*. FEBS Lett. *420*, 161–166.

Motegi, F., Nakano, K., and Mabuchi, I. (2000). Molecular mechanism of myosin-II assembly at the division site in *Schizosaccharomyces pombe*. J. Cell Sci. *113* (Pt 10), 1813–1825.

Nabeshima, K., Nakagawa, T., Straight, A.F., Murray, A., Chikashige, Y., Yamashita, Y.M., Hiraoka, Y., and Yanagida, M. (1998). Dynamics of centromeres during metaphase-anaphase transition in fission yeast: Dis1 is implicated in force balance in metaphase bipolar spindle. Mol. Biol. Cell *9*, 3211–3225.

Naqvi, N., Wong, K.C.Y., Tang, X., and Balasubramanian, M.K. (2000). Type II myosin regulatory light chain relieves auto-inhibition of myosin-heavy-chain function. Nat. Cell Biol. *2*, 855–858.

Oh, Y., Schreiter, J., Nishihama, R., Wloka, C., and Bi, E. (2013). Targeting and functional mechanisms of the cytokinesis-related F-BAR protein Hof1 during the cell cycle. Mol. Biol. Cell *24*, 1305–1320.

Palani, S., Chew, T.G., Ramanujam, S., Kamnev, A., Harne, S., Chapa, Y.L.B., Hogg, R., Sevugan, M., Mishra, M., Gayathri, P., and Balasubramanian, M.K. (2017). Motor activity dependent and independent functions of myosin ii contribute to actomyosin ring assembly and contraction in *Schizosaccharomyces pombe*. Curr. Biol. *27*, 751–757.

Pelham, R.J., and Chang, F. (2002). Actin dynamics in the contractile ring during cytokinesis in fission yeast. Nature *419*, 82–86.

Pollard, T.D. (2017). Nine unanswered questions about cytokinesis. J. Cell Biol. *216*, 3007–3016.

Pollard, T.D., and Wu, J.Q. (2010). Understanding cytokinesis: lessons from fission yeast. Nat. Rev. Mol. Cell Biol. *11*, 149–155.

Proctor, S.A., Minc, N., Boudaoud, A., and Chang, F. (2012). Contributions of turgor pressure, the contractile ring, and septum assembly to forces in cytokinesis in fission yeast. Curr. Biol. *22*, 1601–1608.

Samejima, I., Miller, V.J., Rincon, S.A., and Sawin, K.E. (2010). Fission yeast Mto1 regulates diversity of cytoplasmic microtubule organizing centers. Curr. Biol. *20*, 1959–1965.

Schmidt, M., Bowers, B., Varma, A., Roh, D.-H., and Cabib, E. (2002). In budding yeast, contraction of the actomyosin ring and formation of the primary septum at cytokinesis depend on each other. J. Cell Sci. *115*, 293–302.

Sethi, K., Palani, S., Cortes, J.C., Sato, M., Sevugan, M., Ramos, M., Vijaykumar, S., Osumi, M., Naqvi, N.I., Ribas, J.C., and Balasubramanian, M. (2016). A new membrane protein Sbg1 links the contractile ring apparatus and septum synthesis machinery in fission yeast. PLoS Genet. *12*, e1006383.

Shannon, K.B., and Li, R. (1999). The multiple roles of Cyk1p in the assembly and function of the actomyosin ring in budding yeast. Mol. Biol. Cell *10*, 283–296.

Sipiczki, M. (2000). Where does fission yeast sit on the tree of life? Genome Biol. *1*, REVIEWS1011.

Stark, B.C., James, M.L., Pollard, L.W., Sirotkin, V., and Lord, M. (2013). UCS protein Rng3p is essential for myosin-II motor activity during cytokinesis in fission yeast. PLoS One *8*, e79593.

Takaine, M., Numata, O., and Nakano, K. (2015). An actin-myosin-II interaction is involved in maintaining the contractile ring in fission yeast. J. Cell Sci. *128*, 2903–2918.

Uehara, R., Goshima, G., Mabuchi, I., Vale, R.D., Spudich, J.A., and Griffis, E.R. (2010). Determinants of myosin II cortical localization during cytokinesis. Curr. Biol. *20*, 1080–1085.

Vallen, E.A., Caviston, J., and Bi, E. (2000). Roles of Hof1p, Bni1p, Bnr1p, and Myo1p in cytokinesis in *Saccharomyces cerevisiae*. Mol. Biol. Cell *11*, 593–611.

VerPlank, L., and Li, R. (2005). Cell cycle-regulated trafficking of Chs2 controls actomyosin ring stability during cytokinesis. Mol. Biol. Cell *16*, 2529–2543.

Wang, K., Wloka, C., and Bi, E. (2019). Non-muscle myosin-II is required for the generation of a constriction site for subsequent abscission. iScience *13*, 69–81.

Willet, A.H., Mcdonald, N.A., and Gould, K.L. (2015). Regulation of contractile ring formation and septation in *Schizosaccharomyces pombe*. Curr. Opin. Microbiol. *28*, 46–52.

Wloka, C., Vallen, E.A., Thé, L., Fang, X., Oh, Y., and Bi, E. (2013). Immobile myosin-II plays a scaffolding role during cytokinesis in budding yeast. J. Cell Biol. *200*, 271–286.

Wu, J.Q., Kuhn, J.R., Kovar, D.R., and Pollard, T.D. (2003). Spatial and temporal pathway for assembly and constriction of the contractile ring in fission yeast cytokinesis. Dev. Cell *5*, 723–734.

Wu, J.Q., Sirotkin, V., Kovar, D.R., Lord, M., Beltzner, C.C., Kuhn, J.R., and Pollard, T.D. (2006). Assembly of the cytokinetic contractile ring from a broad band of nodes in fission yeast. J. Cell Biol. *174*, 391–402.

Wu, J.Q., Ye, Y., Wang, N., Pollard, T.D., and Pringle, J.R. (2010). Cooperation between the septins and the actomyosin ring and role of a cell-integrity pathway during cell division in fission yeast. Genetics *186*, 897–915.

Xu, X., and Vogel, B.E. (2011). A secreted protein promotes cleavage furrow maturation during cytokinesis. Curr. Biol. *21*, 114–119.

Zhang, G., Kashimshetty, R., Ng, K.E., Tan, H.B., and Yeong, F.M. (2006). Exit from mitosis triggers Chs2p transport from the endoplasmic reticulum to mother-daughter neck via the secretory pathway in budding yeast. J. Cell Biol. *174*, 207–220.

ISCI, Volume *14*

Supplemental Information

Distinct Roles of Myosin-II Isoforms in Cytokinesis under Normal and Stressed Conditions

Hiroki Okada, Carsten Wloka, Jian-Qiu Wu, and Erfei Bi

Supplemental information

Supplemental Figures

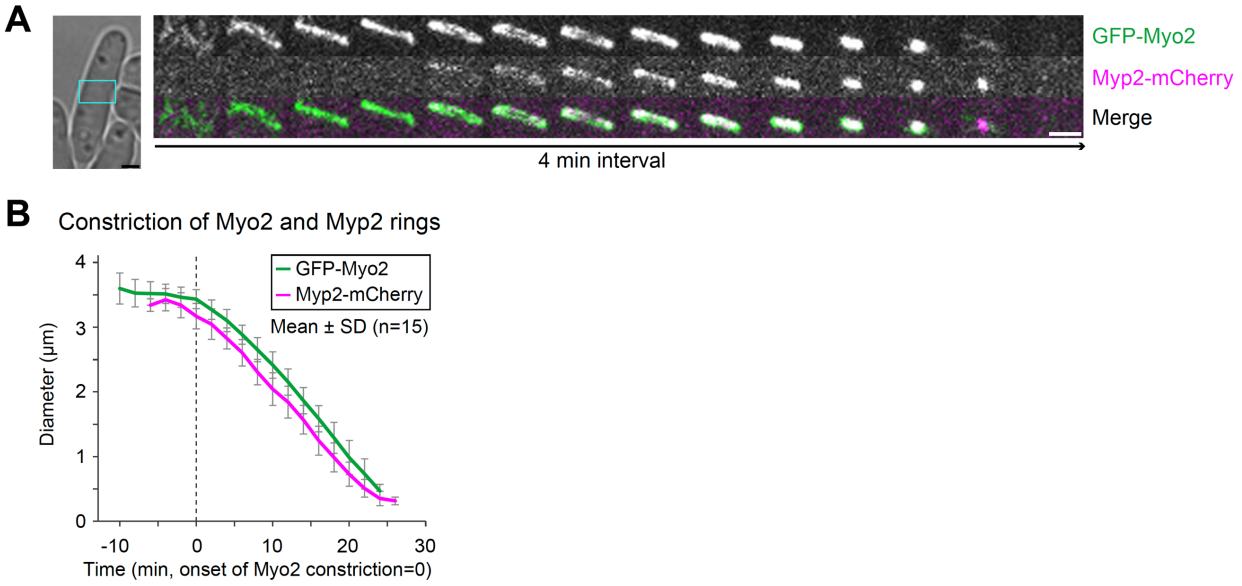

Figure S1. Spatiotemporal offset of constriction of Myo2 and Myp2. Related to Figure 1, and Movie S2.

(A) Cells carrying *GFP-myo2* and *myp2-mCherry* alleles (YCW0153: *GFP-myo2 myp2-mCherry*) were cultured to early exponential phase in the YE5S medium, and then subjected to microscopy. Time lapse images of the ring (right panel) were created from cropped region of a representative cell (cyan box, left panel). Scale bar = 2 μm. (B) Imaging data from (A) were used for analysis. Data on individual cells were aligned according to the onset of Myo2 ring constriction. See also Figure 1, and Movie S2.

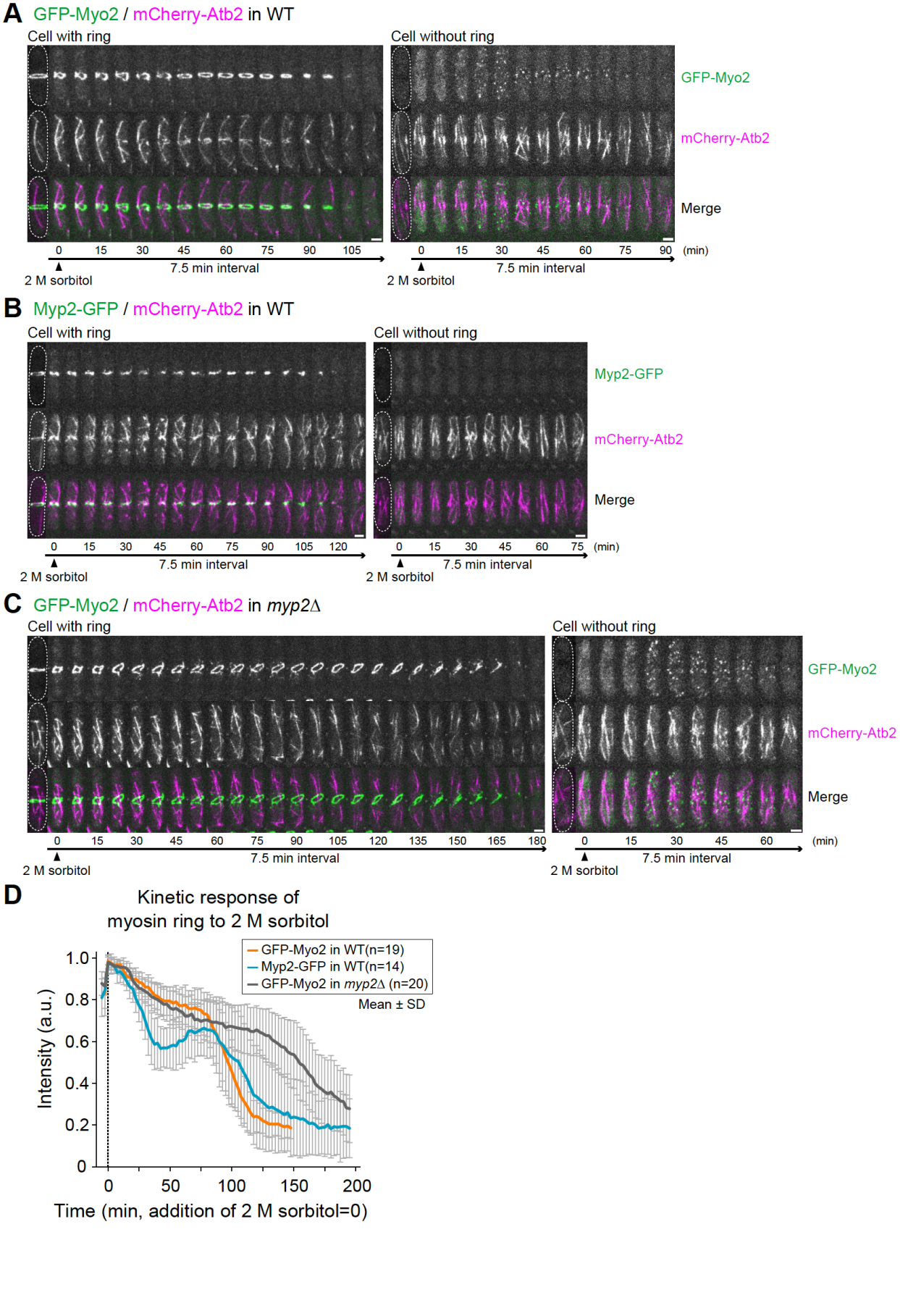
A GFP-Myo2 / mCherry-Atb2 in WT
Cell with ring
Cell without ring
GFP-Myo2
mCherry-Atb2
Merge
0 15 30 45 60 75 90 105
0 15 30 45 60 75 90 (min)
7.5 min interval
2 M sorbitol
B Myp2-GFP / mCherry-Atb2 in WT
Cell with ring
Cell without ring
Myp2-GFP
mCherry-Atb2
Merge
0 15 30 45 60 75 90 105 120
0 15 30 45 60 75 (min)
7.5 min interval
2 M sorbitol
C GFP-Myo2 / mCherry-Atb2 in myp2Δ
Cell with ring
Cell without ring
GFP-Myo2
mCherry-Atb2
Merge
0 15 30 45 60 75 90 105 120 135 150 165 180
0 15 30 45 60 (min)
7.5 min interval
2 M sorbitol
D
Kinetic response of
myosin ring to 2 M sorbitol
GFP-Myo2 in WT(n=19)
Myp2-GFP in WT(n=14)
GFP-Myo2 in myp2Δ (n=20)
Mean ± SD
Intensity (a.u.)
1.0
0.8
0.6
0.4
0.2
0
0 50 100 150 200
Time (min, addition of 2 M sorbitol=0)

Figure S2. Response of Myo2 and Myp2 to 2 M sorbitol treatment. Related to Figure 2, and Movie S3.

(A-C) Time-lapse analysis Myo2 in WT (A), Myp2 in WT (B), and Myo2 in *myp2*Δ (C) was performed on cells of WT strains (YCW0130, and YCW0125), and *myp2*Δ strain (YCW0073). During live-cell imaging, culture medium was changed from YE5S to YE5S containing 2 M sorbitol to induce hyper-osmotic stress response. Representatives of dividing cells with a pre-formed myosin-II ring and interphase cells are shown for each strain. The intensities of Myo2 and Myp2 at the division site from the imaging data as described in Panels A-C are quantified and presented here (D). Scale bar = 2 μm. See also Figure 2, and Movie S3.

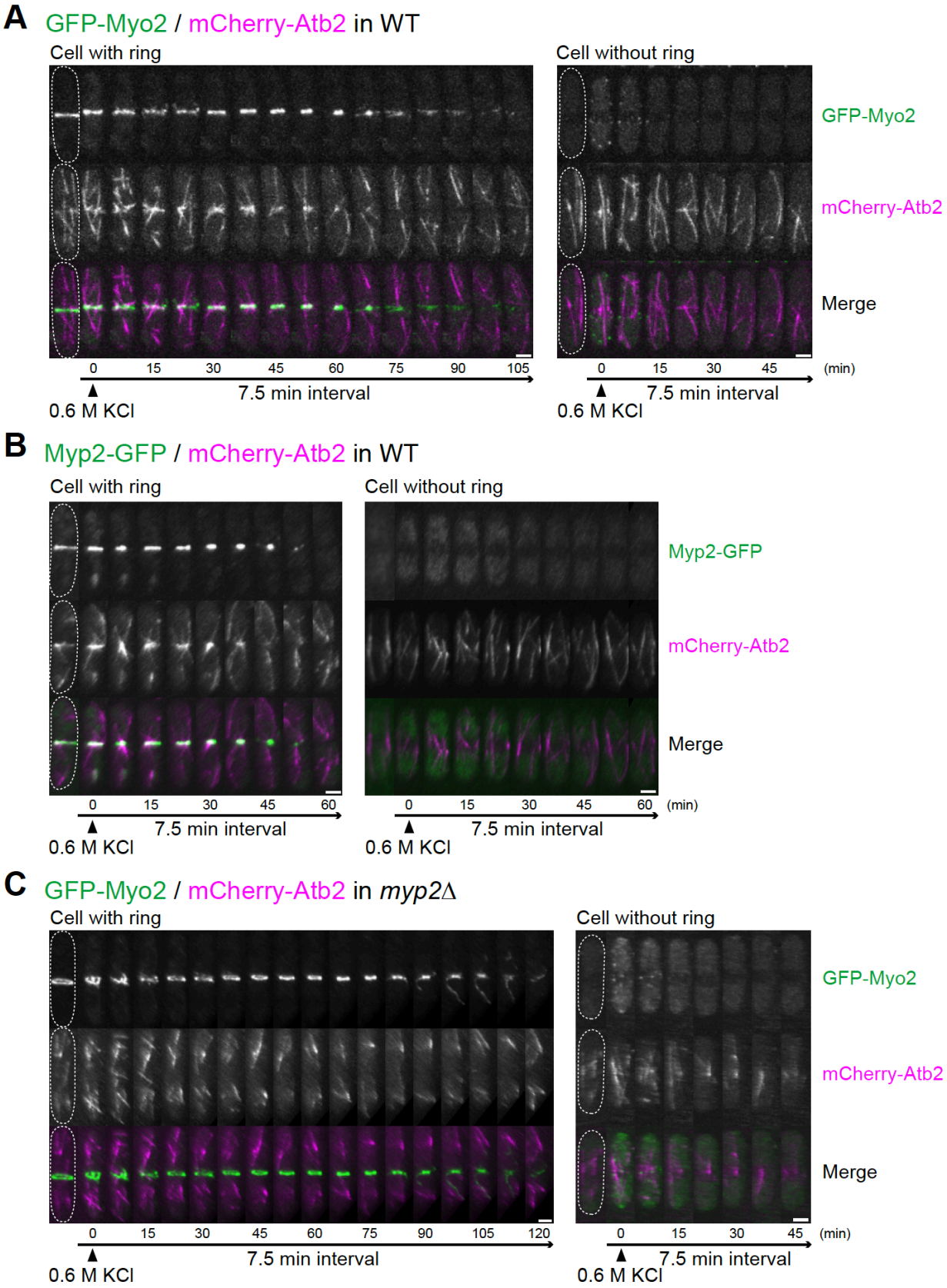
A
GFP-Myo2 / mCherry-Atb2 in WT
Cell with ring
Cell without ring
GFP-Myo2
mCherry-Atb2
Merge
0 15 30 45 60 75 90 105
0 15 30 45
(min)
7.5 min interval
0.6 M KCl
B
Myp2-GFP / mCherry-Atb2 in WT
Cell with ring
Cell without ring
Myp2-GFP
mCherry-Atb2
Merge
0 15 30 45 60
(min)
7.5 min interval
0.6 M KCl
C
GFP-Myo2 / mCherry-Atb2 in myp2Δ
Cell with ring
Cell without ring
GFP-Myo2
mCherry-Atb2
Merge
0 15 30 45 60 75 90 105 120
0 15 30 45
(min)
7.5 min interval
0.6 M KCl

Figure S3. Response of Myo2 and Myp2 to 0.6 M KCl treatment. Related to Figure 2 and Movie S4.

(A-C) Time-lapse analysis Myo2 in WT (A), Myp2 in WT (B), and Myo2 in *myp2*Δ (C) was performed on cells of WT strains (YCW0130, and YCW0125), and *myp2*Δ strain (YCW0073). During live-cell imaging, culture medium was changed from YE5S to YE5S containing 0.6 M KCl to induce high-salt stress response. Representatives of dividing cells with a pre-formed myosin-II ring and interphase cells are shown for each strain. Scale bar = 2 μm. See also Figure 2, and Movie S4.

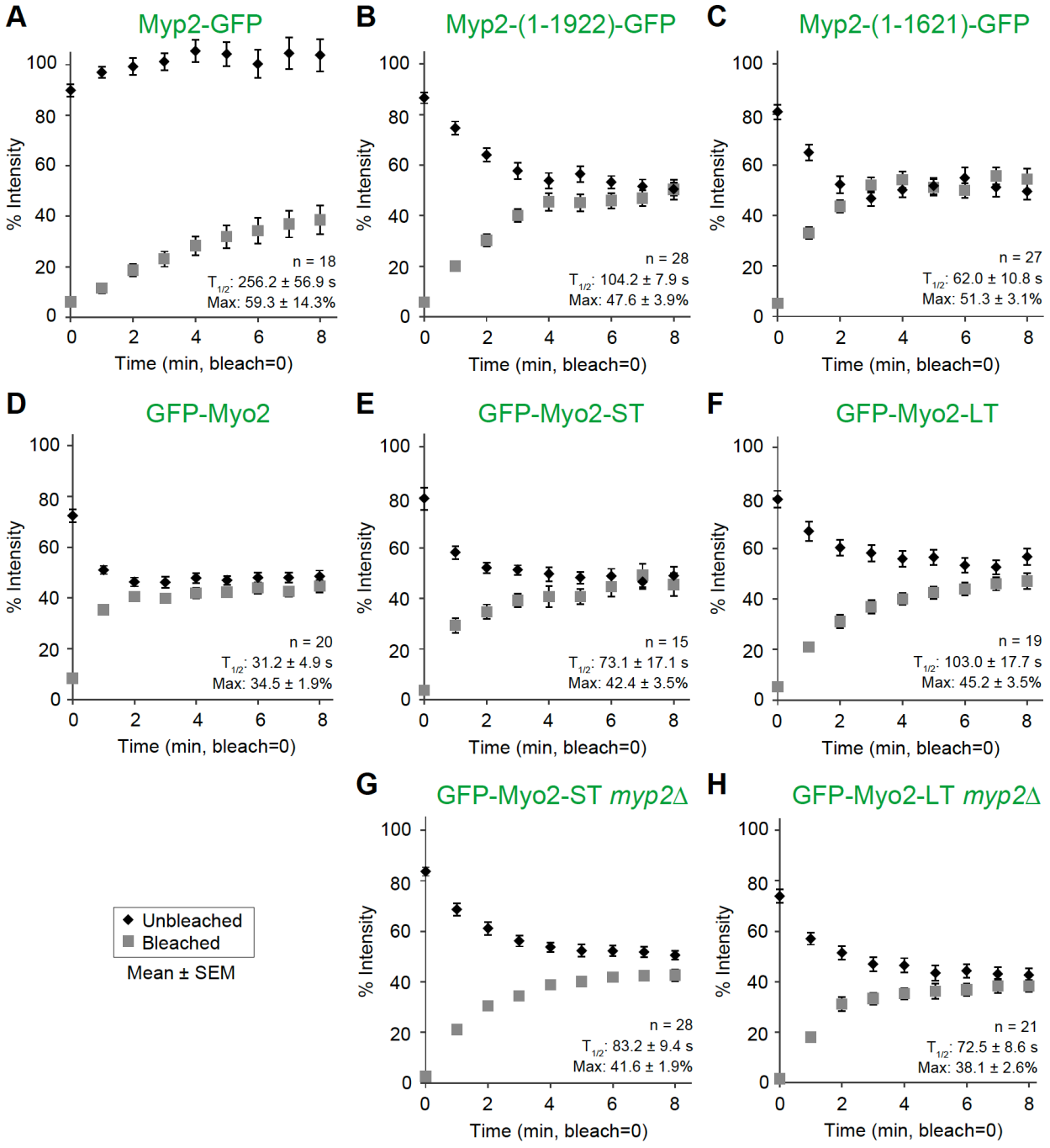
A
Myp2-GFP
% Intensity
Time (min, bleach=0)
n = 18
T1/2: 256.2 ± 56.9 s
Max: 59.3 ± 14.3%
B
Myp2-(1-1922)-GFP
n = 28
T1/2: 104.2 ± 7.9 s
Max: 47.6 ± 3.9%
C
Myp2-(1-1621)-GFP
n = 27
T1/2: 62.0 ± 10.8 s
Max: 51.3 ± 3.1%
D
GFP-Myo2
n = 20
T1/2: 31.2 ± 4.9 s
Max: 34.5 ± 1.9%
E
GFP-Myo2-ST
n = 15
T1/2: 73.1 ± 17.1 s
Max: 42.4 ± 3.5%
F
GFP-Myo2-LT
n = 19
T1/2: 103.0 ± 17.7 s
Max: 45.2 ± 3.5%
G
GFP-Myo2-ST myp2Δ
n = 28
T1/2: 83.2 ± 9.4 s
Max: 41.6 ± 1.9%
H
GFP-Myo2-LT myp2Δ
n = 21
T1/2: 72.5 ± 8.6 s
Max: 38.1 ± 2.6%
Unbleached
Bleached
Mean ± SEM

Figure S4. FRAP analysis of different myosin-II isoforms and their variants. Related to Figures 3, 4 and S6, and Movie S5.

FRAP analysis of WT and mutant myosin-IIs. Four strains including two WT (YCW0130 and YCW0017), two Myp2 truncation mutants (YCW0031 and YCW0032), and four *myo2-myp2* chimera mutants (YCW0166, YCW0175, YCW0190, and YCW0194) were subjected to FRAP analysis. A half of the ring from cells was photo-bleached, and fluorescence recovery in the bleached and unbleached regions was followed and quantified (Mean ± SEM) over time. See also Figures 3, 4 and S6, and Movie S5.

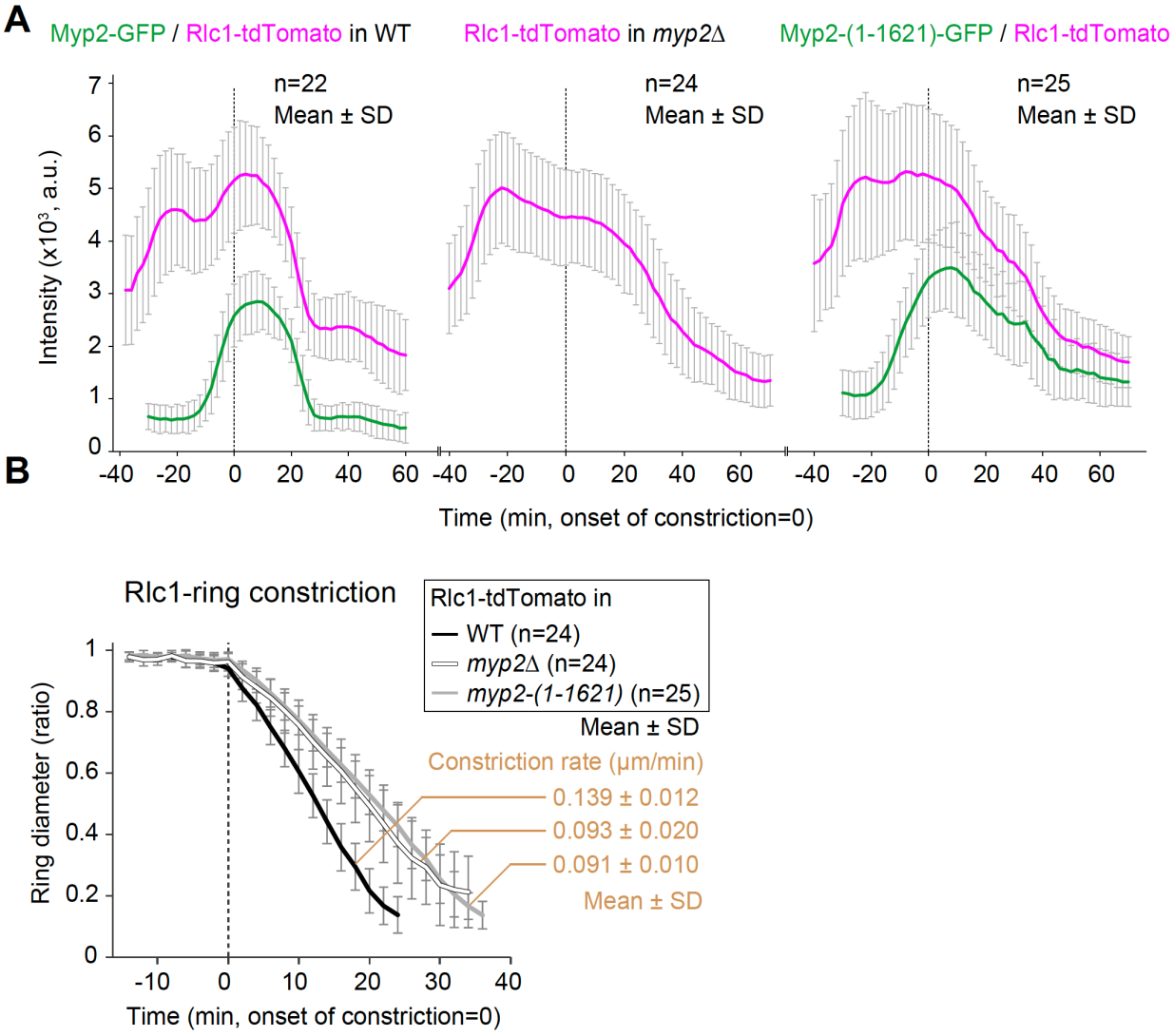

Figure S5. Localization and constriction kinetics of the AMR in *myp2* mutants. Related to Figure 3, and Table S1.

(A-B) Localization and constriction kinetics of the AMR in *myp2* mutants. Contribution of Myp2 to AMR constriction (marked by Rlc1-tdTomato) was examined by time-lapse imaging of cells of WT (YCW0110: *myp2-GFP rlc1-tdTomato*), *myp2*Δ (YCW0112: *myp2*Δ *rlc1-tdTomato*), and *myp2-(1-1621)* (YCW0088: *myp2-(1-1621)-GFP rlc1-tdTomato*) strains. Imaging data on individual cells were aligned according to the onset of Rlc1 ring constriction. See also Figure 3, and Table S1.

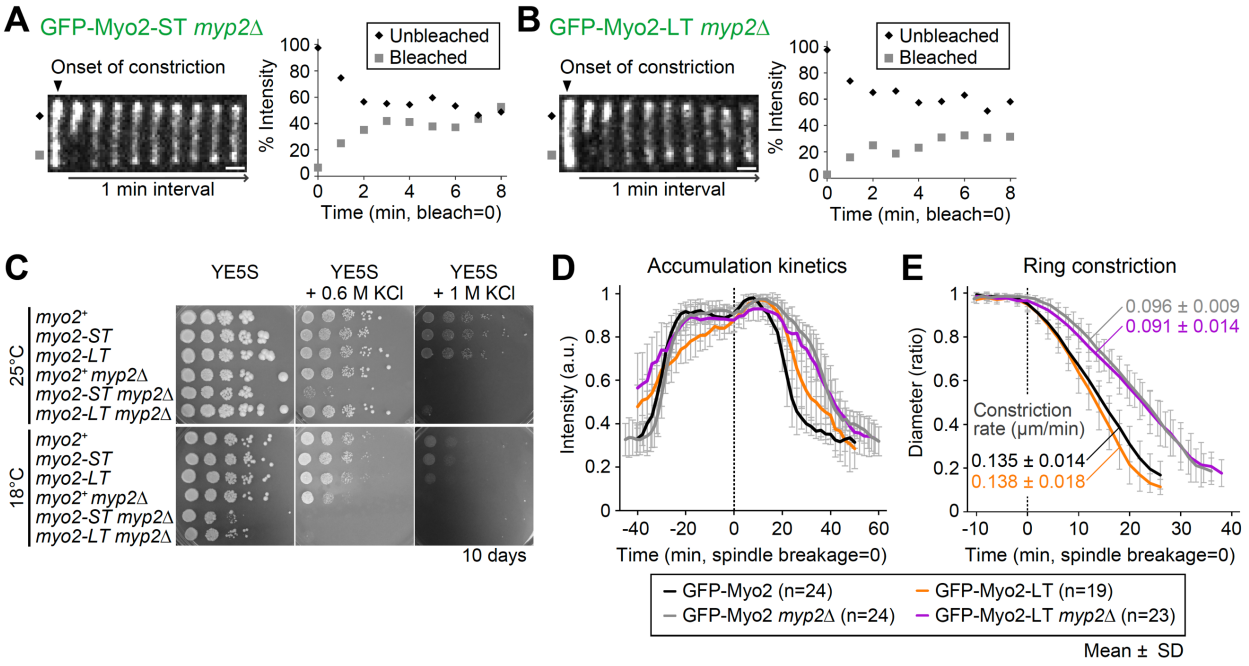

Figure S6. Myosin chimera phenotypes are independent of the endogenous *myp2*$^{+}$. Related to Figure 4 and S4, and Movie S5.

(A-B) FRAP analysis of *myo2-myp2* chimera in *myp2*Δ background (YCW0190, and YCW0194). Scale bar = 1 μm. (C) Growth of strains of WT (YCW0077: *GFP-myo2*), *myo2-ST* [YCW0147: *GFP-myo2-myp2-(1923-2104)*], *myo2-LT* [YCW0197: *GFP-myo2-myp2-(1622-2104)*], *myp2*Δ (YCW0023: *myp2*Δ *GFP-myo2*), *myo2-ST myp2*Δ [YCW0191: *myp2*Δ *GFP-myo2-myp2-(1923-2104)*], and *myo2-LT myp2*Δ [YCW0196: *myp2*Δ *GFP-myo2-myp2-(1622-2104)*] was examined on YE5S plate with or without potassium chloride. See also Figures 4 and S4, and Movie S5.

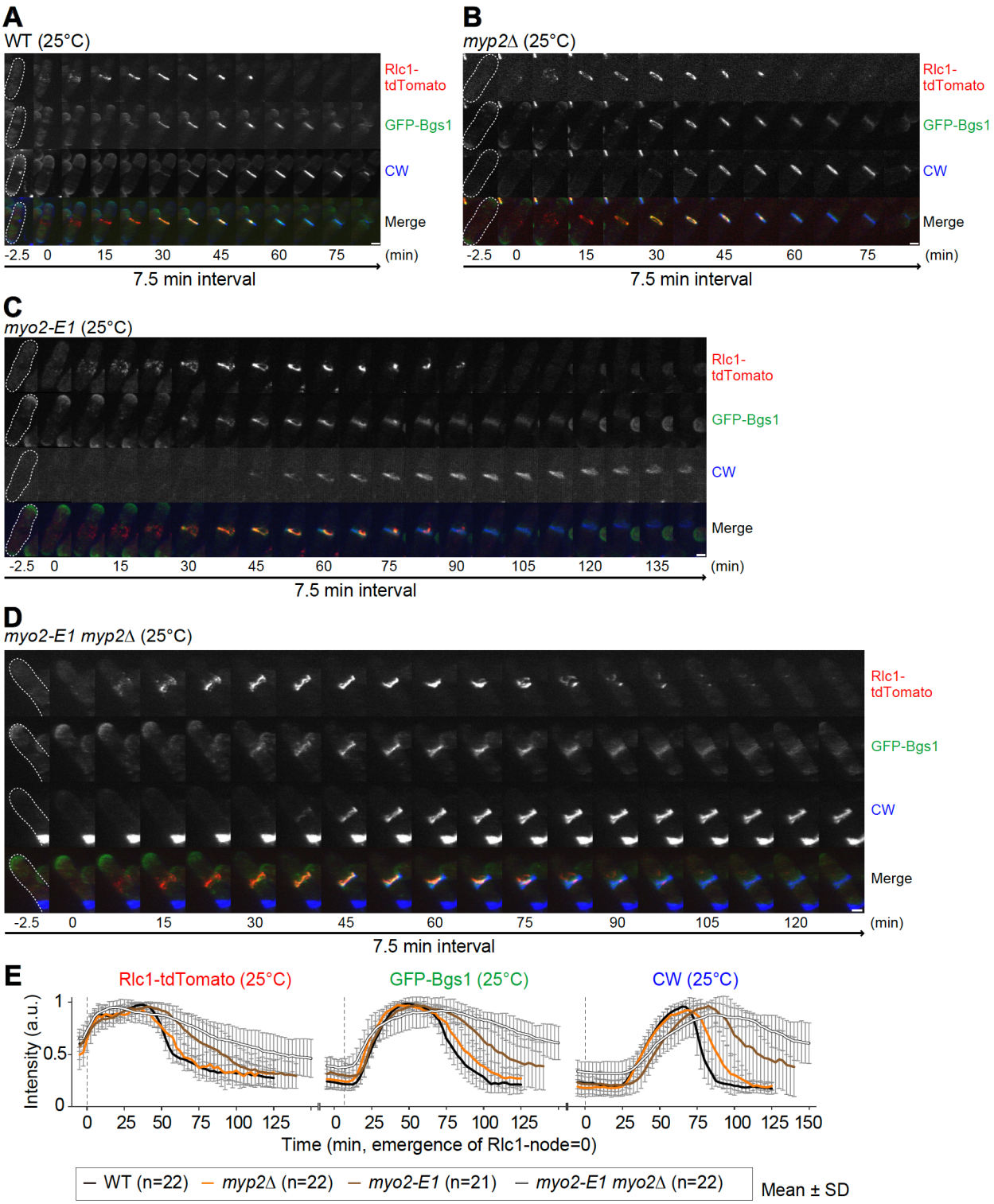
A
WT (25°C)
Rlc1-tdTomato
GFP-Bgs1
CW
Merge
-2.5 0 15 30 45 60 75 (min)
7.5 min interval
B
myp2Δ (25°C)
Rlc1-tdTomato
GFP-Bgs1
CW
Merge
-2.5 0 15 30 45 60 75 (min)
7.5 min interval
C
myo2-E1 (25°C)
Rlc1-tdTomato
GFP-Bgs1
CW
Merge
-2.5 0 15 30 45 60 75 90 105 120 135 (min)
7.5 min interval
D
myo2-E1 myp2Δ (25°C)
Rlc1-tdTomato
GFP-Bgs1
CW
Merge
-2.5 0 15 30 45 60 75 90 105 120 (min)
7.5 min interval
E
Rlc1-tdTomato (25°C)
GFP-Bgs1 (25°C)
CW (25°C)
Intensity (a.u.)
1
0.5
0
0 25 50 75 100 125
0 25 50 75 100 125
0 25 50 75 100 125 150
Time (min, emergence of Rlc1-node=0)
WT (n=22)
myp2Δ (n=22)
myo2-E1 (n=21)
myo2-E1 myo2Δ (n=22)
Mean ± SD

Figure S7. Myo2 and Myp2 play distinct roles in AMR assembly and constriction as well as in guiding Bgs1-mediated PS formation at 25°C. Related to Figure 5 and Movie S6.

(A-D) The montage created from a representative cell of each strain imaged in Figure 5A. The strains were: WT (YCW0117), *myp2*Δ (YCW0043), *myo2-E1* (YCW0044), and *myo2-E1 myp2*Δ (YCW0047). Scale bar = 2 μm. (E) Kinetics of AMR formation, Bgs1 cargo accumulation, and PS formation at 25°C. See also Figure 5, and Movie S6.

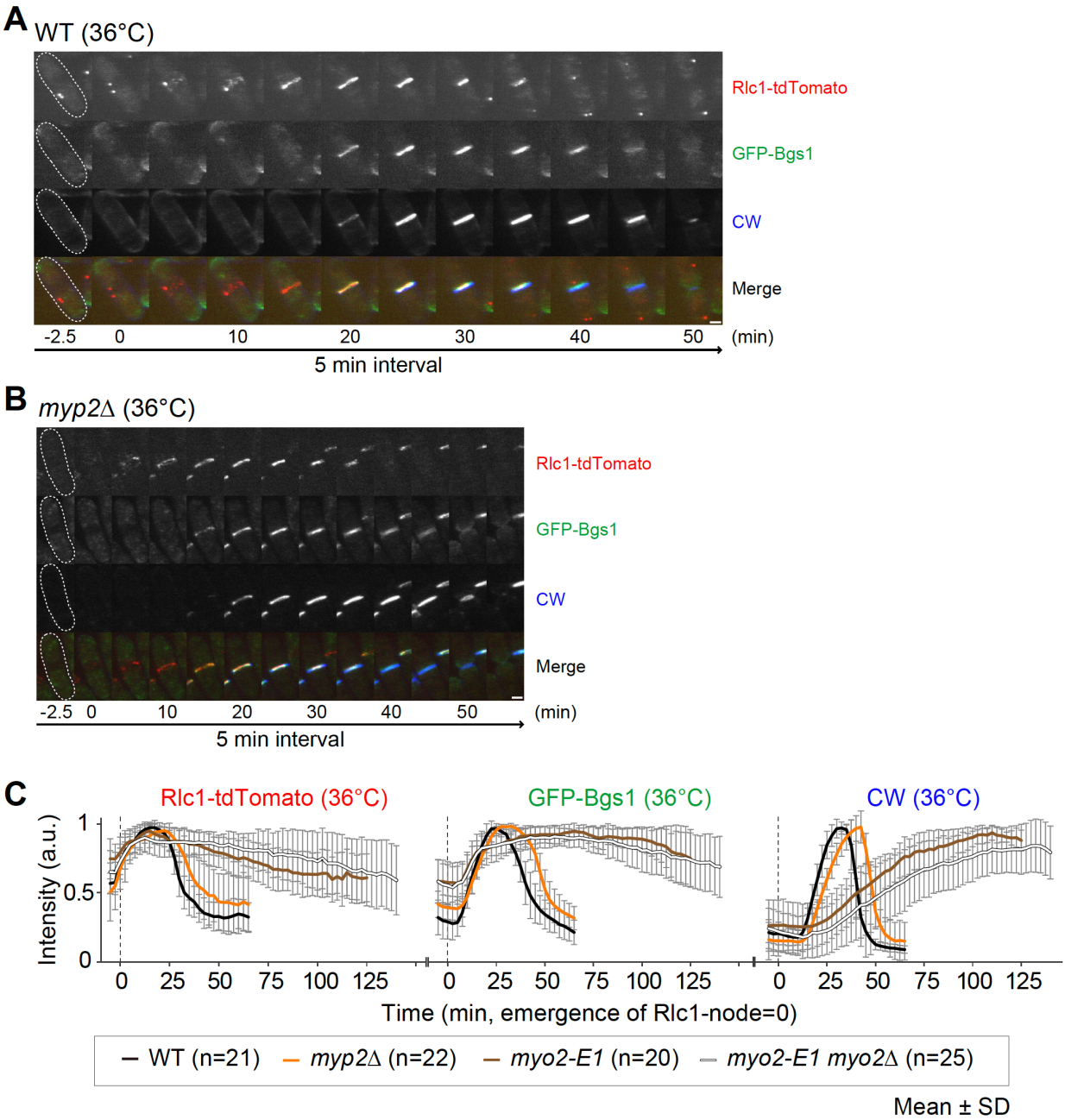
A
WT (36°C)
Rlc1-tdTomato
GFP-Bgs1
CW
Merge
-2.5 0 10 20 30 40 50 (min)
5 min interval
B
myp2Δ (36°C)
Rlc1-tdTomato
GFP-Bgs1
CW
Merge
-2.5 0 10 20 30 40 50 (min)
5 min interval
C
Rlc1-tdTomato (36°C)
GFP-Bgs1 (36°C)
CW (36°C)
Intensity (a.u.)
1
0.5
0
0 25 50 75 100 125
Time (min, emergence of Rlc1-node=0)
WT (n=21)
myp2Δ (n=22)
myo2-E1 (n=20)
myo2-E1 myo2Δ (n=25)
Mean ± SD

Figure S8. Myo2 and Myp2 play distinct roles in AMR assembly and constriction as well as in guiding Bgs1-mediated PS formation at 36°C. Related to Figure 5 and Movie S6.

(A-B) The montage created from a representative cell of each strain imaged in Figure 5D. The strains were: WT (YCW0117), and *myp2*Δ (YCW0043). Scale bar = 2 μm. (C) Kinetics of AMR formation, Bgs1 cargo accumulation, and PS formation at 36°C. See also Figure 5, and Movie S6.

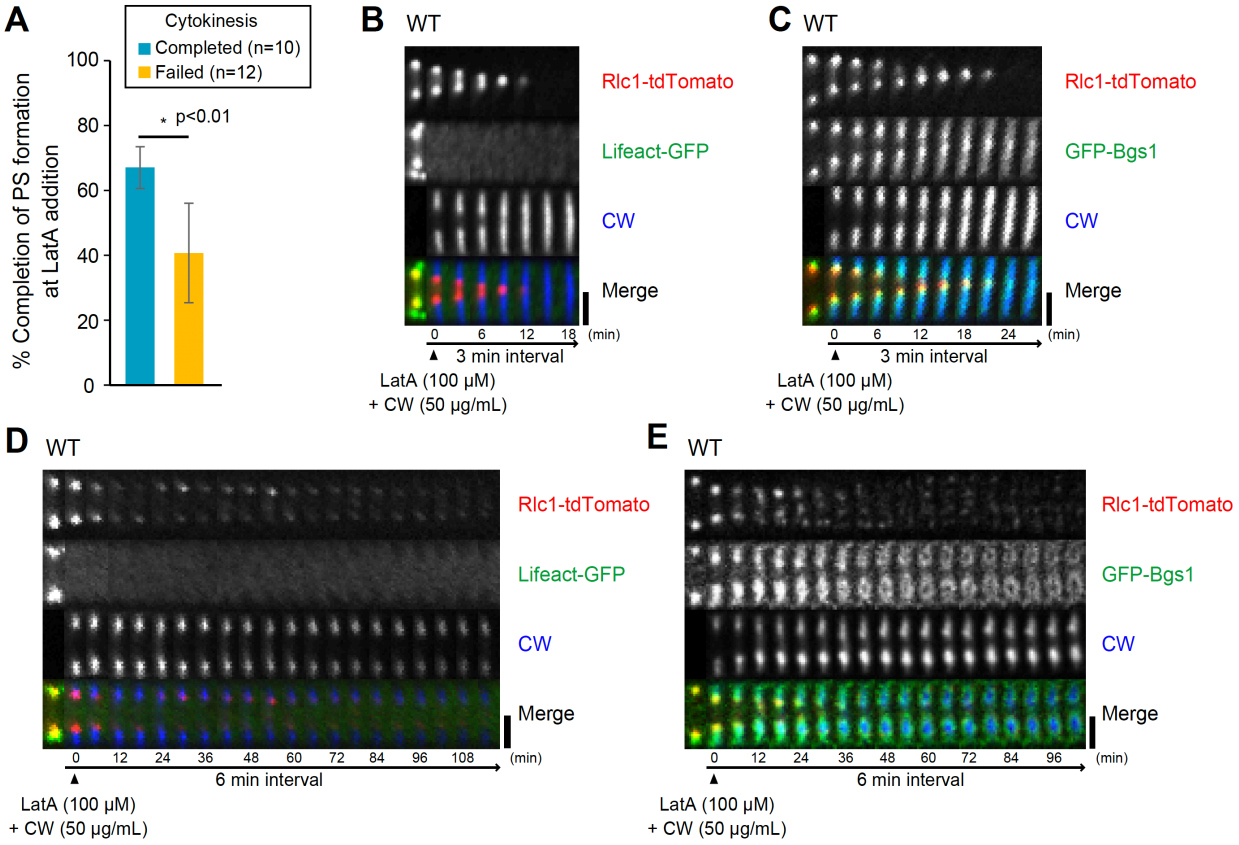

Figure S9. Actin filaments are required for maintaining myosin-II concentration at the division site during early stage of AMR constriction. Related to Figure 7 and Movie S8.
(A) PS formation and cytokinesis under 100 μM LatA. Progress of PS formation was measured as the ratio of septum length (CW marked) to the diameter of the division site from the dividing cells imaged in Figure 7D and 7E. (B-E) The montage created for the division site of a representative cell from a mixed culture of two WT strains (YCW0079 and YCW0117). Scale bar = 2 μm. See also Figure 7 and Movie S8.

LEGENDS FOR SUPPLEMENTAL MOVIES

Movie S1. Localization of Myo2 (WT, and Myo2-Myp2 chimeras) and Myp2 (WT, and C-terminal truncations) during the cell cycle. Related to Figures 1, 3, and 4.

Movie S2. Spatiotemporal offset of Myo2 and Myp2 constriction. Related to Figures 1 and S1.

Movie S3. Behaviors of Myo2 (in WT and *myp*2Δ cells) and Myp2 under stress conditions (1 M KCl or 2 M sorbitol). Related to Figures 2, and S2.

Movie S4. Behaviors of Myo2 (in WT and *myp*2Δ cells) and Myp2 under stress condition (0.6 M KCl). Related to Figures 2, and S3.

Movie S5. FRAP analysis of Myo2 (WT, and Myo2-Myp2 chimeras) and Myp2 (WT, and C-terminal truncations) during cytokinesis. Related to Figures 3, 4, and S6.

Movie S6. Localization of Rlc1 and Bgs1, and PS formation in WT, *myp2*Δ, *myo2-E1*, and *myo2-E1 myp2*Δ strains at permissive (25°C) or restrictive (36°C) temperature. Related to Figures 5, S7, and S8.

Movie S7. Localization of Rlc1 and Bgs1, and PS formation in Myo2-depleted cells in the presence (*N-degron-myo2*) or absence (*N-degron-myo2 myp2*Δ) of Myp2. Related to Figure 6.

Movie S8. Localization of Rlc1, Actin, and Bgs1, and PS formation in the presence of LatA. Related to Figures 7 and S9.

Table S1: Constriction rates of myosin-IIs and their variants in different strains. Related to Figures 2F, 4G, and S5B.

			Constriction rate (μm/min)			Relative constriction rate (%)	
Genotype	Marker	Medium	Mean	SD	n	to WT	to YE5S
WT	GFP-Myo2	YE5S	0.135	0.014	24	100.0	
*myp2*Δ	GFP-Myo2	YE5S	0.096*	0.009	24	70.6	
myo2-ST	GFP-Myo2-ST	YE5S	0.133	0.024	18	98.5	
myo2-LT	GFP-Myo2-LT	YE5S	0.138	0.018	19	102.2	
*myo2-LT myp2*Δ	GFP-Myo2-LT	YE5S	0.091*	0.014	23	69.5	
WT	GFP-Myo2	YE5S + 0.6 M KCl	0.051‡	0.007	15	100.0	37.8
*myp2*Δ	GFP-Myo2	YE5S + 0.6 M KCl	0.052‡	0.005	22	102.0	54.2
WT	Myp2-GFP	YE5S	0.118	0.015	24	100.0	
myp2(1-1621)	Myp2(1-1621)-GFP	YE5S	0.089*	0.017	23	75.4	
myp2(1-1922)	Myp2(1-1922)-GFP	YE5S	0.091*	0.013	24	77.1	
WT	Rlc1-tdTomato	YE5S	0.139	0.012	24	100.0	
*myp2*Δ	Rlc1-tdTomato	YE5S	0.093*	0.020	24	66.9	
myp2-(1-1621)	Rlc1-tdTomato	YE5S	0.091*	0.010	25	65.5	

* $p<0.01$ by student's t-test (versus WT), ‡ $p<0.01$ by student's t-test (versus YE5S)

Table S2: Genetic interactions of *myp2* mutations with other mutations affecting cytokinesis. Related to Figure 3.

Strain	Temperature (°C)[a]				
	23	**25**	**30**	**32**	**36**
*myp2*Δ	+++	+++	+++	+++	++
myp2-mEGFP	+++	+++	+++	+++	+++
myp2(1-1621)	+++	+++	+++	+++	+++
myp2(1-1922)	+++	+++	+++	+++	+++
cdc4-s16	+	++	++	++	ND
cdc4-s16 myp2-mEGFP	+	++	++	++	ND
*cdc4-s16 myp2*Δ	-	-	+	+	ND
cdc4-s16 myp2(1-1621)	-	+	+	++	ND
cdc4-s16 myp2(1-1922)	-	+	++	++	ND
myo2-E1	ND	+++	+++	++	++
*myo2-E1 myp2*Δ	ND	++	+	+	-
myo2-E1 myp2(1-1621)	ND	++	++	+	-
myo2-E1 myp2(1-1922)	ND	++	++	+	-
cdc11-123	ND	+++	+++	++	-
*cdc11-123 myp2*Δ	ND	+++	++	+	-
cdc11-123 myp2(1-1621)	ND	+++	++	+	-
cdc11-123 myp2(1-1922)	ND	+++	++	+	-
*myo51*Δ	ND	+++	+++	+++	+++
*myo51*Δ *myp2-mEGFP*	ND	+++	+++	+++	++
*myo51*Δ *myp2*Δ	ND	++	++	++	++
*myo51*Δ *myp2(1-1621)*	ND	++	++	++	++
*myo51*Δ *myp2(1-1922)*	ND	+++	+++	+++	++

[a]Growth on YE5S plates and color of colonies on YE5S + phloxin B plates was tested at various temperatures. "+++" similar to wt (phloxin pink); "++" slow growth and small colonies (phloxin red); "+" very slow growth and tiny colonies (phloxin red); "-" inviable or no colony formation (phloxin dark red). ND, no data.

Table S3. Strains, primers, and plasmids used in this study. Related to Figures 1-7, S1-9, and Movies S1-8.

REAGENT or RESOURCE	SOURCE	IDENTIFIER
Experimental Models: Organisms/Strains		
Schizosaccharomyces pombe: Strain YCW0015: *h⁻ myp2-GFP(S65T)-kanMX6 ade6-M210 leu1-32 ura4-D18*	(Wu et al., 2003)	JW706
S. pombe: Strain YCW0017: *h⁺ myp2-mEGFP-kanMX6 ade6-M210 leu1-32 ura4-D18 mCherry-atb2:hphMX6*	This study	
S. pombe: Strain YCW0018: *h⁺ myp2-GFP(S65T)-kanMX6 ade6-M210 leu1-32 ura4-D18 mCherry-atb2:hphMX6*	This study	
S. pombe: Strain YCW0023: *h⁻ kanMX6-Pmyo2-GFP(S65T)-myo2 myp2-Δ2::kanMX6 ade6-M210 leu1-32 ura4-D18*	(Wu et al., 2003)	JW780-1
S. pombe: Strain YCW0029: *h⁻ myp2-(AA1-1621)-mEGFP-kanMX6 ade6-M210 leu1-32 ura4-D18*	This study	
S. pombe: Strain YCW0030: *h⁻ myp2-(AA1-1922)-mEGFP-kanMX6 ade6-M210 leu1-32 ura4-D18*	This study	
S. pombe: Strain YCW0031: *h⁻ myp2-(AA1-1621)-mEGFP-kanMX6 mCherry-atb2:hphMX6 ade6-M210 leu1-32 ura4-D18*	This study	
S. pombe: Strain YCW0032: *h⁺ myp2-(AA1-1922)-mEGFP-kanMX6 mCherry-atb2:hphMX6 ade6-M210 leu1-32 ura4-D18*	This study	
S. pombe: Strain YCW0043: *h⁻ GFP-bgs1-leu1⁺ bgs1Δ::ura4⁺ rlc1-tdTomato-natMX6 ade6-M210 leu1-32 ura4-D18 myp2-Δ2::kanMX6*	This study	JW5313
S. pombe: Strain YCW0044: *h⁻ GFP-bgs1-leu1⁺ bgs1Δ::ura4⁺ rlc1-tdTomato-natMX6 ade6-M210 leu1-32 ura4-D18 myo2-E1*	This study	JW5314
S. pombe: Strain YCW0045: *h⁻ GFP-bgs1-leu1⁺ bgs1Δ::ura4⁺ kanMX6-Pmyo2-N-degron-myo2 myp2-Δ2::kanMX6 ade6-M210 leu1-32 ura4-D18*	This study	JW5315
S. pombe: Strain YCW0046: *h⁻ GFP-bgs1-leu1⁺ bgs1Δ::ura4⁺ kanMX6-Pmyo2-N-degron-myo2 rlc1-tdTomato-natMX6 ade6-M210 leu1-32 ura4-D18*	This study	JW5316
S. pombe: Strain YCW0047: *h⁻ GFP-bgs1-leu1⁺ bgs1Δ::ura4⁺ rlc1-tdTomato-natMX6 myp2-Δ2::kanMX6 myo2-E1 ade6-M210 leu1-32 ura4-D18*	This study	JW5324
S. pombe: Strain YCW0052: *h⁻ myo2-E1 ade6-216 ura4-D18 leu1-32 his3-D1*	D. McCollum	YDM74
S. pombe: Strain YCW0053: *h⁺ cdc4-s16-F3 ade6-M210 his7-366 leu1-32 ura4-D18*	(Wu et al., 2010)	JW400
S. pombe: Strain YCW0054: *h⁻ myp2-Δ2::kanMX6 ade6-M210 leu1-32 ura4-D18*	(Wu et al., 2003)	JW703-1
S. pombe: Strain YCW0056: *h⁺ myo51Δ::ura4⁺ ade6-M210 leu1-32 ura4-D18*	(Win et al., 2001)	JW1273 (213)
S. pombe: Strain YCW0057: *h⁻ cdc11-123 leu1-32 ura4-D18 ade6-210*	This study	JW1366
S. pombe: Strain YCW0058: *h⁻ cdc11-123 leu1-32 ura4-D18 ade6-210*	This study	JW3358-1
S. pombe: Strain YCW0059: *h⁺ cdc4-s16-F3 myp2-Δ2::kanMX6 ade6-M210 his7-366? leu1-32 ura4-D18*	This study	JW5681-1
S. pombe: Strain YCW0060: *h⁻ cdc4-s16-F3 myp2-Δ2::kanMX6 ade6-M210 his7-366? leu1-32 ura4-D18*	This study	JW5682-1

S. pombe: Strain YCW0061: *h+ cdc4-s16-F3 myp2-(aa1-1621)-mEGFP-kanMX6 ade6-M210 his7-366? leu1-32 ura4-D18*	This study	JW5683-1
S. pombe: Strain YCW0062: *h+ cdc4-s16-F3 myp2-(aa1-1922)-mEGFP-kanMX6 ade6-M210 his7-366? leu1-32 ura4-D18*	This study	JW5684-1
S. pombe: Strain YCW0063: *h+ cdc11-123 myp2-Δ2::kanMX6 ade6-210 leu1-32 ura4-D18*	This study	JW5692-1
S. pombe: Strain YCW0064: *h- cdc11-123 myp2-(aa1-1621)-mEGFP-kanMX6 ade6-210 leu1-32 ura4-D18*	This study	JW5693-1
S. pombe: Strain YCW0065: *h+ cdc11-123 myp2-(aa1-1922)-mEGFP-kanMX6 ade6-210 leu1-32 ura4-D18*	This study	JW5694-1
S. pombe: Strain YCW0066: *h+ myo51Δ::ura4+ myp2-mEGFP-kanMX6 ade6-210 leu1-32 ura4-D18*	This study	JW5695-1
S. pombe: Strain YCW0067: *h- myo51Δ::ura4+ myp2-(aa1-1621)-mEGFP-kanMX6 ade6-210 leu1-32 ura4-D18*	This study	JW5696-1
S. pombe: Strain YCW0068: *h- myo51Δ::ura4+ myp2-(aa1-1922)-mEGFP-kanMX6 ade6-210 leu1-32 ura4-D18*	This study	JW5697-1
S. pombe: Strain YCW0069: *h- myo51Δ::ura4+ myp2-Δ2::kanMX6 ade6-210 leu1-32 ura4-D18*	This study	JW5698-1
S. pombe: Strain YCW0070: *h+ myo2-E1 myp2-Δ2::kanMX6 ade6 leu1-32 ura4-D18 his3-D1?*	This study	JW5703-1
S. pombe: Strain YCW0071: *h+ myo2-E1 myp2-(aa1-1621)-mEGFP-kanMX6 ade6 leu1-32 ura4-D18 his3-D1?*	This study	JW5704-1
S. pombe: Strain YCW0072: *h- myo2-E1 myp2-(aa1-1922)-mEGFP-kanMX6 ade6 leu1-32 ura4-D18 his3-D1?*	This study	JW5705-1
S. pombe: Strain YCW0073: *h- kanMX6-Pmyo2-GFP(S65T)-myo2 myp2-Δ2::kanMX6 ade6-M210 leu1-32 ura4-D18 mCherry-atb2:hphMX6*	This study	
S. pombe: Strain YCW0077: *h+* kanMX6-Pmyo2-mEGFP-myo2 ade6-M210 leu1-32 ura4-D18	(Coffman et al., 2009)	JW1109
S. pombe: Strain YCW0079: *h- kanMX6-P3nmt1-mEGFP-lifeact rlc1-tdTomato-natMX6 ade6-M210 leu1-32 ura4-D18*	(Coffman et al., 2009)	JW1666-1
S. pombe: Strain YCW0088: *h- myp2-(AA1-1621)-mEGFP-kanMX6 rlc1-tdTomato-natMX6 ade6-M210 leu1-32 ura4-D18*	This study	
S. pombe: Strain YCW0110: *h+ myp2-mEGFP-kanMX6 rlc1-tdTomato-natMX6 ade6-M210 leu1-32 ura4-D18*	This study	
S. pombe: Strain YCW0112: *h+ myp2-Δ2::kanMX6 rlc1-tdTomato-natMX6 ade6-M210 leu1-32 ura4-D18*	This study	
S. pombe: Strain YCW0117: *h+ GFP-bgs1-leu1+ bgs1Δ::ura4+ rlc1-tdTomato-natMX6 ade6-M210 leu1-32 ura4-D18*	This study	
S. pombe: Strain YCW0125: *h+ myp2-mEGFP-kanMX6 mCherry-atb2:hphMX6 ade6-210 leu1-32 ura4-D18*	This study	
S. pombe: Strain YCW0130: *h- kanMX6-Pmyo2-mEGFP-myo2 ade6-M210 leu1-32 ura4-D18 mCherry-atb2:hphMX6*	This study	
S. pombe: Strain YCW0147: *h+ kanMX6-Pmyo2-mEGFP-myo2-myp2-(AA1923-2104)-natMX6 ade6-M210 leu1-32 ura4-D18*	This study	
S. pombe: Strain YCW0153: *h- myp2-mCherry-kanMX6 kanMX6-Pmyo2-mEGFP-myo2 ade6-M210 leu1-32 ura4-D18*	This study	
S. pombe: Strain YCW0166: *h- kanMX6-Pmyo2-mEGFP-myo2-myp2-(AA1923-2104)-natMX6 mCherry-atb2:hphMX6 ade6-M210 leu1-32 ura4-D18*	This study	

S. pombe: Strain YCW0175: *h⁻ kanMX6-Pmyo2-mEGFP-myo2-myp2-(AA1622-2104)-natMX6 mCherry-atb2:hphMX6 ade6-M210 leu1-32 ura4-D18*	This study	
S. pombe: Strain YCW0190: *h⁻ myp2-Δ2::kanMX6 kanMX6-Pmyo2-mEGFP-myo2-myp2-(AA1923-2104)-natMX6 mCherry-atb2:hphMX6 ade6-M210 leu1-32 ura4-D18*	This study	
S. pombe: Strain YCW0191: *h⁻ myp2-Δ2::kanMX6 kanMX6-Pmyo2-mEGFP-myo2-myp2-(AA1923-2104)-natMX6 ade6-M210 leu1-32 ura4-D18*	This study	
S. pombe: Strain YCW0194: *h⁻ myp2-Δ2::kanMX6 kanMX6-Pmyo2-mEGFP-myo2-myp2-(AA1622-2104)-natMX6 mCherry-atb2:hygR ade6-M210 leu1-32 ura4-D18*	This study	
S. pombe: Strain YCW0196: *h⁻ myp2-Δ2::kanMX6 kanMX6-Pmyo2-mEGFP-myo2-myp2-(AA1622-2104)-natMX6 ade6-M210 leu1-32 ura4-D18*	This study	
S. pombe: Strain YCW0197: *h⁻ kanMX6-Pmyo2-mEGFP-myo2-myp2-(AA1622-2104)-natMX6 ade6-M210 leu1-32 ura4-D18*	This study	
S. pombe: Strain YCW0199: *h⁺ myp2-mEGFP-kanMX6 alp4-TagRFP-kanMX mCherry-atb2:hphMX6 ade6-210 leu1-32 ura4-D18*	This study	
S. pombe: Strain YCW0201: *h⁺ kanMX6-Pmyo2-mEGFP-myo2-myp2-(AA1622-2104)-natMX6 alp4-TagRFP-kanMX ade6-M210 leu1-32 ura4-D18*	This study	
Oligonucleotides		
Myp2 truncation with GFP tagging: Tagging at AA 1922: AGATGACTTACTATCATCATTAGTTGAACGCATAAA ACAGATCGAAATGTTTGCGCTAAAAACTCAAAAACG GATCCCCGGGTTAATTAA	This study	N/A
Myp2 truncation with GFP tagging: Tagging at AA 1621: TGATGGTAGTATAACTAATTATTCTGGAGAAGAAGA AACCGAGTGGTTGCAAGAAGAAGTTAATATAATGCG GATCCCCGGGTTAATTAA	This study	N/A
Myp2 truncation with GFP tagging: Myp2-Stop+70bp.Rev: AATTTTAAATTCATGAACTAATAATTTACATCATCTT AAAAAATACATGTCGAGTCTTTGGGAAGCTTGGGAA TTCGAGCTCGTTTAAAC	This study	N/A
Myp2 truncation with GFP tagging: Myp2-Aa1400.Bp4200.Fwd: TACTGGGCTGAAACCTTTGT	This study	N/A
Myp2 truncation with GFP tagging: Myp2-AaSTOP+5Bp.Bp6320.Rev: ATGTCGAGTCTTTGGGAAGC	This study	N/A
Gap repair cloning for construction of pRS316-myo2(aa1218-1526)-myp2(aa1923-2104)-tADH1-NatR-tmyo2 and pRS316-myo2(aa1218-1526)-myp2(aa1622-2104)-tADH1-NatR-tmyo2: F265-MCS-MYO2(1218): CTCTAGAACTAGTGGATCCCAAGCTTTCGTTGGCGA GCTCCGAGAATAAAGATCTCTCTA	This study	F265
Gap repair cloning for construction of pRS316-myo2(aa1218-1526)-myp2(aa1923-2104)-tADH1-NatR-tmyo2: R242-Myo2(1526)-Myp2(1923): TGCGGCGCGCAACTCATCTTCAAGGCTTGC	This study	R242

Gap repair cloning for construction of pRS316-myo2(aa1218-1526)-myp2(aa1923-2104)-tADH1-NatR-tmyo2: F266-Myo2(1526)-Myp2(1923): AAGATGAGTTGCGCGCCGCAGATAGTAATAATCATCGAGAAGAAAATCTTCAACTGCATC	This study	F266
Gap repair cloning for construction of pRS316-myo2(aa1218-1526)-myp2(aa1923-2104)-tADH1-NatR-tmyo2 and pRS316-myo2(aa1218-1526)-myp2(aa1622-2104)-tADH1-NatR-tmyo2: R243-Myp2(2104)-ADH1term: AGAAATTCGCCTACCTTAGAACGCTAGGCGAACGATTGGA	This study	R243
Gap repair cloning for construction of pRS316-myo2(aa1218-1526)-myp2(aa1923-2104)-tADH1-NatR-tmyo2 and pRS316-myo2(aa1218-1526)-myp2(aa1622-2104)-tADH1-NatR-tmyo2: F267-Myp2(2104)-ADH1term: TCTAAGGTAGGCGAATTTCTTATGATTTATGATTTTTATT	This study	F267
Gap repair cloning for construction of pRS316-myo2(aa1218-1526)-myp2(aa1923-2104)-tADH1-NatR-tmyo2 and pRS316-myo2(aa1218-1526)-myp2(aa1622-2104)-tADH1-NatR-tmyo2: R244-TEFterm-Myo2-term: TCATTTAACTCAGTATAGCGACCAGCATTCACATACGATT	This study	R244
Gap repair cloning for construction of pRS316-myo2(aa1218-1526)-myp2(aa1923-2104)-tADH1-NatR-tmyo2 and pRS316-myo2(aa1218-1526)-myp2(aa1622-2104)-tADH1-NatR-tmyo2: F268-TEFterm-Myo2-term: CGCTATACTGAGTTAAATGATTTTGTAATGATGAAACCTT	This study	F268
Gap repair cloning for construction of pRS316-myo2(aa1218-1526)-myp2(aa1923-2104)-tADH1-NatR-tmyo2 and pRS316-myo2(aa1218-1526)-myp2(aa1622-2104)-tADH1-NatR-tmyo2: R245-Myo2term-MCS: GCCCCCCCTCGAGGTCGACGGGATCCCGTGCAGTAACTGAAATTTCTATTGAAGGCTTGA	This study	R245
Gap repair cloning for construction of pRS316-myo2(aa1218-1526)-myp2(aa1622-2104)-tADH1-NatR-tmyo2: F270-Myo2(1526)-Myp2(1622): AAGATGAGTTGCGCGCCGCAAAGATAAAGGAGCTTACTTCTACAGTTAACAAGTACCGCG	This study	F270
Myo2 sequencing: F269-Myo2-seq(aa1190): TACAAACTTTCAGGAACTTTC	This study	F269
Recombinant DNA		
Plasmid: pFA6a-mEGFP-kanMX	Addgene	Cat #: 105146
Plasmid: pFA6a-link-yoEGFP-clonNat	This study	E2375
Plasmid: pRS316	(Sikorski and Hieter, 1989)	
Plasmid: pRS316-myo2(aa1218-1526)-myp2(aa1923-2104)-tADH1-NatR-tmyo2	This study	E2493
Plasmid: pRS316-myo2(aa1218-1526)-myp2(aa1622-2104)-tADH1-NatR-tmyo2	This study	E2494

TRANSPARENT METHODS

Yeast media and culture conditions

The fission yeast *S. pombe* strains used in this study are listed in **Table S3**. Standard *S. pombe* media and methods were used (Moreno et al., 1991). The YE5S medium consists of 0.5% yeast extract (Sunrise Science Products, San Diego, CA), 3% dextrose (Sunrise Science Products), and 0.0225% of each of the supplements: adenine (Sunrise Science Products), histidine (Sunrise Science Products), leucine (Sunrise Science Products), uracil (Sunrise Science Products), and lysine (Sunrise Science Products). All strains were grown at 25°C unless otherwise indicated. Stock solutions of 20 mM LatA (in DMSO, Wako, Osaka, Japan), and/or 1% (w/v) CW (in distilled water, Sigma, St. Louis, MO) were added to medium to a final concentration as indicated.

Constructions of strains

We used standard genetic (tetrad dissection, and random spore analysis) and PCR-based gene targeting methods to construct the strains used in this study (Moreno et al., 1991, Bahler et al., 1998). The strains carrying C-terminal tagging of Myp2 with GFP were constructed following the standard PCR-based approach. The PCR condition for a 100 µl reaction is: 6 µl ExTaq Polymerase (Takara Bio, Kusatsu, Japan), 2.5 mM for each dNTP, 2 mM $MgCl_2$, 0.5 µg tagging vector DNA, 2 µM for each of the defined forward and reverse primers, and distilled water (to fill to 100 µl), 25 cycles of 98°C for 12 sec, 62°C for 25 sec, and 72°C for 155 sec. The construction of the *N-degron-myo2* strain under the control of *myo2* promoter was described before (Laporte et al., 2011). The strains carrying Myo2-Myp2 chimeras were constructed as follows. Two plasmids pRS316-myo2(aa1218-1526)-myp2(aa1923-2104)-tADH1-NatR-tmyo2, which harbors Myp2 tail domain (residue 1923-2104) followed by *ADH1* terminator and *NatMX6* cassette flanked by chromosomal $myo2^+$ sequence for gene targeting (~0.9k and ~0.4k base pairs upstream and downstream of stop codon of $myo2^+$, respectively), and pRS316-myo2(aa1218-1526)-myp2(aa1622-2104)-tADH1-NatR-tmyo2, which is identical to the above plasmid except length of Myp2 tail domain (residue 1622-2104), were constructed by gap repair cloning. Each DNA fragment module were prepared by PCR and sub-cloned into a multiple cloning site of vector pRS316 via homologous recombination in the wild-type budding yeast

BY4741 (Brachmann et al., 1998). These plasmids were digested with BamHI, and a 3.3- or 4.2-kb fragment from the respective plasmid was used to transform fission yeast cells. Transformants were selected by resistance to nourseothricin (clonNAT), and subsequently confirmed by sequencing.

Yeast growth assay

To determine sensitivity of cells to potassium chloride, cells were grown in YE5S medium at 25°C for 12 hours. Cell culture was diluted with fresh YE5S medium to the 0.3 OD_{600}. The cell suspension was subjected to 10-fold serial dilutions and inoculated onto YE5S plate, or YE5S plate containing 0.6, or 1 M potassium chloride (Calbiochem). After incubation at 25°C or 18°C for 10 days, the cell growth on the plate was recorded.

Quantification of glucan deposition in PS

To determine the relative glucan levels at the division site (data presented in Figure 6B), cells were grown to exponential phase in liquid YE5S at 25°C, diluted 20-fold into fresh medium, and incubated at 36°C for 12 hours. Cells were pelleted by centrifugation and washed once with YE5S with 50 μg/ml CW (Sigma). Cells were then resuspended in the same medium, and subjected to the microscope experiments. For quantification of CW intensities, the integrated density at the division site was measured by subtracting the background intensity from the total intensity of the region of interest covered by ImageJ-drawn polygon.

Quantification of myosin-II spot number and intensity

To determine the abundance of myosin-II spot in each strain (data presented in Figure 4H), cells were grown to early exponential phase in liquid YE5S at 25°C. The culture was split into two parts, which were incubated at 25°C and 36°C, respectively, for 6 hours. Cells were concentrated by centrifugation, and subjected to the imaging and spot counting. For quantification of spot intensities (data presented in Figure 4I), the integrated density of the spot was measured by subtracting the background intensity from the total intensity of the region of interest covered by ImageJ-drawn polygon.

FRAP

To perform FRAP (data presented in Figure 1E-F, Figure 2B-C), a diode-pumped 405nm violet-blue laser (model DL405-050-O CrystaLaser, Reno, NV, USA) was used to apply defined, pixel-sized, spots on the area to be bleached. The laser intensity was kept to a minimum where bleaching still occurred in order to reduce phototoxicity. Maximum projections were created and analyzed with NIH ImageJ. In ImageJ, a polygon was drawn encircling the bleached area in order to calculate the integrated density within the area over time. Data were plotted using GraphPad Prism 7 and half-life was determined using the one phase-association function in the GraphPad.

Imaging and data analysis

For FRAP analysis, cells were grown at room temperature to exponential phase in YE5S medium. To make an agarose pad, molten YE5S medium (contains 2% agarose) was poured into a silicone mold set on a microscope slide and covered with a cover glass, and then left for 10 minutes for solidification. After gentle removal of the cover glass, fresh cells were spotted directly onto the pad. A new cover glass was then placed on the pad, and samples were used for imaging at room temperature. A spinning-disk confocal imaging system that consists of a spinning-disk scan head (model CSU-X1, Yokogawa, Tokyo, Japan) and a microscope (model IX81, Olympus, Tokyo, Japan) equipped with a 100×/1.40 NA oil objective (model UPlanSApo 100x/1.40 Oil, Olympus) and an EMCCD camera (model iXon X3 897, Andor Technology, Belfast, UK) was used. MetaMorph ver. 7.8.10.0 (Molecular Devices, Downingtown, PA, USA) was used for hardware control and image acquisition. For excitation, diode lasers (488 nm for GFP and 561 nm for RFP) controlled via laser merge module (model LMM5, Spectral Applied Research, Richmond Hill, Ontario, Canada) were used. A typical z-stack consisted of 13 × 0.5 μm optical sections.

All other imaging experiments presented in this study were performed as follows. Cells were cultured to exponential phase at 25°C in YE5S medium, pelleted by centrifugation, and placed on cover glass underneath YE5S agarose pad. A thermalization chip (Cherry Biotech, Rennes, France) was then installed on top of the cover glass to control the temperature during live imaging. A microfluidic chip (Cherry Biotech) was used to perform an imaging experiment that required drug perfusion. Cells were first primed with 2 mg/ml concanavalin A (Sigma), and then

loaded to the chamber of the chip. Cells were immobilized on the poly-lysine-coated chamber bottom. Time-lapse microscopy was performed using an imaging system that consists of a microscope (model Eclipse Ti-U, Nikon, Tokyo, Japan) equipped with a confocal scanner unit (model CSU-X1, Yokogawa), a 100×/1.49NA oil objective (model CFI Apo TIRF 100×, Nikon), a temperature controller (model CherryTemp, Cherry Biotech), and an EMCCD camera (either model QuantEM: 512SC or Evolve 512 Delta, Photometrics, Tucson, AZ, USA). Solid-state lasers for excitation (405 nm for CW, 488 nm for GFP, and 561 nm for RFP) were housed in a launch (model ILE-400, Spectral Applied Research). The imaging system was controlled by MetaMorph ver. 7.8.10.0 (Molecular Devices). Images were taken every 1.5, 2, or 3 min with z-stacks ranging from 11 × 1-1.2 μm. A sum or maximum projection was created with NIH ImageJ (1.51j). For quantification of fluorescence intensities, the integrated density at the division site was calculated by subtracting the fluorescence intensity in background area from the total intensity in an ImageJ-drawn polygon covering the division site. For calculating the rate of ring constriction, we manually measured the myosin ring diameter during cytokinesis from the maximum projection of a time-lapse series, and then calculated the slope of the curve using the diameters from 4 or 5 time points that cover the midpoint of constriction. Data analyses were performed with Microsoft Excel and R (ver. 3.0.1).

QUANTITATION AND STATSITICAL ANALYSIS

For statistical analysis of the glucan levels (related to Figures 6B), intensity of myosin-II spot (related to Figure 4I), and progression of PS formation (related to Figure S9A), two-sided unpaired t-test (assuming unequal variances) was performed. "n" refers to the number of cells analyzed unless indicated otherwise.

Supplemental references

BAHLER, J., WU, J. Q., LONGTINE, M. S., SHAH, N. G., MCKENZIE, A., 3RD, STEEVER, A. B., WACH, A., PHILIPPSEN, P. & PRINGLE, J. R. 1998. Heterologous modules for efficient and versatile PCR-based gene targeting in *Schizosaccharomyces pombe*. *Yeast* 14**,** 943-51.

BRACHMANN, C. B., DAVIES, A., COST, G. J., CAPUTO, E., LI, J., HIETER, P. & BOEKE, J. D. 1998. Designer deletion strains derived from *Saccharomyces cerevisiae* S288C: a

useful set of strains and plasmids for PCR-mediated gene disruption and other applications. *Yeast* 14**,** 115-32.

COFFMAN, V. C., NILE, A. H., LEE, I. J., LIU, H. & WU, J. Q. 2009. Roles of formin nodes and myosin motor activity in Mid1p-dependent contractile-ring assembly during fission yeast cytokinesis. *Mol. Biol. Cell* 20**,** 5195-210.

LAPORTE, D., COFFMAN, V. C., LEE, I. J. & WU, J. Q. 2011. Assembly and architecture of precursor nodes during fission yeast cytokinesis. *J Cell Biol,* 192**,** 1005-21.

MORENO, S., KLAR, A. & NURSE, P. 1991. Molecular genetic analysis of fission yeast *Schizosaccharomyces pombe*. *Methods Enzymol.* 194**,** 795-826.

SIKORSKI, R. S. & HIETER, P. 1989. A system of shuttle vectors and yeast host strains designed for efficient manipulation of DNA in *Saccharomyces cerevisiae*. *Genetics* 122**,** 19-27.

WIN, T. Z., GACHET, Y., MULVIHILL, D. P., MAY, K. M. & HYAMS, J. S. 2001. Two type V myosins with non-overlapping functions in the fission yeast *Schizosaccharomyces pombe*: Myo52 is concerned with growth polarity and cytokinesis, Myo51 is a component of the cytokinetic actin ring. *J. Cell Sci.* 114**,** 69-79.

WU, J. Q., KUHN, J. R., KOVAR, D. R. & POLLARD, T. D. 2003. Spatial and temporal pathway for assembly and constriction of the contractile ring in fission yeast cytokinesis. *Dev. Cell* 5**,** 723-34.

WU, J. Q., YE, Y., WANG, N., POLLARD, T. D. & PRINGLE, J. R. 2010. Cooperation between the septins and the actomyosin ring and role of a cell-integrity pathway during cell division in fission yeast. *Genetics* 186**,** 897-915.